

UC San Diego

UC San Diego Electronic Theses and Dissertations

Title

Composite bone substitutes prepared by two methods

Permalink

<https://escholarship.org/uc/item/36p7t5t4>

Authors

Lee, Hoe Yun

Lee, Hoe Yun

Publication Date

2012

Peer reviewed|Thesis/dissertation

UNIVERSITY OF CALIFORNIA, SAN DIEGO

Composite bone substitutes prepared by two methods

A Thesis submitted in partial satisfaction of the requirements
for the degree Master of Science

in

Materials Science and Engineering

by

Hoe Y Lee

Committee in charge:

Professor Joanna McKittrick, Chair
Professor Ratnesh Lal
Professor Vlado A. Lubarda

2012

©

Hoe Y Lee, 2012

All rights reserved.

The Thesis of Hoe Y Lee is approved, and it is acceptable in
quality and form for publication or microfilm and electronically:

Chair

University of California, San Diego

2012

Two roads diverged in a yellow wood,
And sorry I could not travel both
And be one traveler, long I stood
And looked down one as far as I could
To where it bent in the undergrowth;

Then took the other, as just as fair,
And having perhaps the better claim,
Because it was grassy and wanted wear;
Though as for that the passing there
Had worn them really about the same,

And both that morning equally lay
In leaves no step had trodden black.
Oh, I kept the first for another day!
Yet knowing how way leads on to way,
I doubted if I should ever come back.

I shall be telling this with a sigh
Somewhere ages and ages hence:
Two roads diverged in a wood, and I-
I took the one less traveled by,
And that has made all the difference.

Robert Frost

TABLE OF CONTENTS

TTITLE PAGE.....	iii
SIGNATURE PAGE.....	iii
SIGNATURE PAGE.....	iii
EPIGRAPH	iv
TABLE OF CONTENTS	v
LIST OF FIGURES	vii
LIST OF TABLES	xiii
ACKNOWLEDGEMENTS	xiv
ABSTRACT OF THE THESIS	xv
INTRODUCTION	1
BACKGROUND	14
Desirable Implant Characteristics	27
Introduction to Freeze-casting.....	29
EXPERIMENTAL METHOD	38
Natural hydroxyapatite scaffolds	38
Synthetic hydroxyapatite scaffolds by freeze casting	38
Polymer Infiltration	42
Compression Testing.....	43
Physical & Chemical Characterization	43
RESULTS & DISCUSSION.....	45
Natural Scaffolds	45

Natural scaffold composite.....	49
Synthetic scaffold.....	51
Synthetic scaffold composite	58
Summary of Infiltrated Scaffolds	60
CONCLUSION	63
Recommendations for Future Work.....	64
REFERENCES.....	65

LIST OF FIGURES

Figure 1. Radiographs showing the effects of unstable internal fixation. On the left is a radiograph taken postoperatively and on the right is another taken 8 months after the initial surgery [1].....	2
Figure 2. The x-ray radiographs of the skull on the left show an example of a titanium skull implant used after a decompression surgery [3CAB]. The x-ray image on the far right is of a fractured tibia that required internal fixation using a combination of screws and plates [4].....	3
Figure 3. Anatomical locations of autograft harvest sites [11]. Bone can be taken from the iliac crest located on the pelvis, the tibia in the leg, or the radius located in the forearm. .	4
Figure 4. Grafton DBM is available in various shapes and sizes (manufacturer image)....	5
Figure 5. Microstructure comparison of Bio-Oss® (left) and human cancellous bone (right) (SEM 50x). The Bio-Oss® produced from bovine bone has features (i.e. porosity) that are very similar to human bone (Manufacturer images).....	7
Figure 6. Microstructure comparison of Biocoral® (50% porosity) (a) and human cancellous bone (b). Like Bio-Oss®, Biocoral® possess microstructural features that mimic those of human cancellous bone.	8
Figure 7. Series of radiographs showing bone development after removal of a giant cell tumor at the distal end of the tibia. a) Before surgery. b) Immediately after surgery. Visible are the hydroxyapatite granules packed into the void left by tumor removal. c) 3 years after surgery [32].	10
Figure 8. Poly(lactic-co-glycolic-acid) scaffold (Osteofoam™) obtained by phase inversion. [42].....	11

Figure 9. Hierarchical structure of bone showing the various length scales involved in building up to whole bone.....	14
Figure 10. Transmission electron micrograph of the hydroxyapatite crystals from human bone (put scale bar) (taken from Wein) [63].	16
Figure 11. A schematic illustration of the nanostructure of collagen. (taken from Rho) [64].....	17
Figure 12. TEM brightfield image of an isolated collagen fibril showing the characteristic banding pattern of type-I collagen. The inset image (top right) is a selected area electron diffraction (SAED) pattern. The pattern is diffuse, suggesting that the the electron dense phase is amorphous CaP. The sample was not stained (taken from Olszta) [26].	18
Figure 13. Schematic illustrations of the four types of collagen fibril arrangements. a) Array of parallel fibrils. b) Woven fiber structure. c) Plywood-like structure present in lamellar bone. d) Radial fibril arrays (adapted from Weinan).....	19
Figure 14. Scanning electron images of human fetal bone comparing parallel (a) fibrils to (b) woven fibrils. The fibrils in the parallel arrangement are densely packed and well ordered, whereas the fibrils in the woven arrangement are unorganized and loosely packed with visibly empty pockets (taken from Su) [74].	21
Figure 15. a) Diagram of the lacunae spaces (yellow) connected by a network of channels known as canaliculi. b) A partial section of an osteon. The lines indicate the fiber orientation of each lamella. c) The protruding osteon displays the multiple layers that it is composed of and is shown surrounded by other osteons within the context of cortical...	23
Figure 16. Young's modulus and hardness as a function of the lamella in an osteon. Lamellae #1 is nearest to the Haversian canal and #10 is furthest. Both mechanical	

properties decrease moving outward from the center of the osteon (adapted from Rho)	
[80].	24
Figure 17. SEM images of cancellous bone taken from a femoral head (a, b) and the femoral condyle (c). These images illustrate the various morphologies of cancellous bone: a) rods, b) plates, c) plate-like columnar (taken from Gibson) [85].	26
Figure 18. Radiographs of a 51-year-old woman's hip implants illustrating the effects of stress shielding. (a) Postoperative (b) Taken 2 years after implantation. There is a marked loss in bone density near the femoral head. (taken from Engh) [98].	29
Figure 19. Schematic of particle–freezing-front interactions. (Adapted from Wegst)	
[113].	31
Figure 20. Illustration showing ice growth during freeze-casting. Through control of the thermal gradient, the interlamellar spacing (λ) can be modified. $A = \text{constant}$.	32
Figure 21. Effects of additive addition to the microstructure of freeze-cast ceramics. a) Water, b) water + 20 wt% glycerol, and c) water + 60 wt% dioxane (taken from Fu)	
[102].	33
Figure 22. Microstructural evolution of freeze-cast HA on addition of different concentrations of gelatin. (a) 0 wt.%, (b) 2 wt.%, and (c) 6 wt.%. The solid loading was 50 wt.% HA (taken from Fu) [117]	34
Figure 23. Effects of glycerol concentration on the microstructure of the sintered HA sample (a), (b) 5 wt. %; (c), (d) 20 wt. %. (The cross section is perpendicular to the freezing direction.) (taken from Fu) [118]	35

Figure 24. Effects of dioxane concentration on the microstructure of the sintered HA sample (a), (b) 30 wt. %; (c), (d) 60 wt. %. (The cross section is perpendicular to the freezing direction.) (taken from Fu) [118].....	36
Figure 25. Microstructures of (a), (b) vertical, and (c), (d) horizontal cross-sectional views in the sintered Al ₂ O ₃ , unidirectionally solidified body. Arrows in the figure indicate the solidification direction. (taken from Araki) [119].....	36
Figure 26. Typical SEM micrographs of the porous calcium phosphate scaffolds produced at various freezing times of 1 day ((A),(D)), 2 days ((B),(E)), and 3 days ((C),(F)), showing highly aligned pore structures. The top ((A),(B),(C)) and bottom ((D),(E),(F)) images represent the pore structures developed parallel and normal to	37
Figure 27. Particle size analysis of the Trans-Tech hydroxyapatite powder. The average particle diameter was 646.4 nm.	39
Figure 28. Dimensioned drawing of copper cold finger, PTFE mold, and copper lid.....	41
Figure 29. Schematic diagram of the freeze-casting apparatus.	42
Figure 30. a) Micrograph of untreated bovine cancellous bone. b) SEM image of natural scaffold (heat treated at 1325°C).	45
Figure 31. X-ray diffraction pattern of cancellous bone heated at 1325°C for 3 hours (natural scaffold) compared with hydroxyapatite reference peaks (PDF# 00-009-0432). 46	
Figure 32. Stress-strain curves for cancellous bone. As relative density increases, Young's modulus and compressive strength increase. The strain at which the cell walls touch and densification occurs decreases (taken from Gibson) [85].	47
Figure 33. Representative behavior of natural scaffold under compressive loading ($\epsilon = 0.001$ mm/sec).....	48

Figure 34. Representative curves of the compressive behavior of pure PMMA compared against natural scaffold composite. The PMMA exhibited higher strength (80MPa) while the natural scaffold composite had a higher Young's modulus (55 MPa).....	50
Figure 35. SEM image PMMA infiltrated natural hydroxyapatite scaffold. Circled in red is a smooth channel formerly occupied by part of the natural scaffold.	50
Figure 36. X-ray diffraction pattern of synthetic scaffold treated at 1350°C for 3 hours compared with hydroxyapatite reference peaks (PDF# 00-009-0432).	52
Figure 37. SEM images of synthetic scaffold fabricated from 20 vol. % HA and cooled at various rates. The cooling rate for each row is denoted by the inset box.	53
Figure 38. SEM images of synthetic scaffold fabricated from 30 vol.% HA and cooled at various rates. The cooling rate for each row is denoted by the inset box.	54
Figure 39. SEM images of synthetic scaffold fabricated from 35 vol.% HA and cooled at various rates. The cooling rate for each row is denoted by the inset box.	55
Figure 40. Representative stress vs. strain plot of the synthetic scaffolds (30 vol.% cooled at rates of 1, 5, and 10°C/min).	56
Figure 41. (a) The strength of the synthetic scaffold increases logarithmically as a function of the cooling rate. (b)	57
Figure 42. (a) Synthetic freeze-casted hydroxyapatite (HA) scaffold infiltrated with PMMA. (b) Fracture surface of the synthetic HA-PMMA composite after compressive failure. The light bands are the inorganic HA phase and the dark bands are the organic PMMA.	59
Figure 43. Log-log Plot of the relative strength versus the relative density of the synthetic scaffolds and natural scaffold composite.	61

Figure 44. Plot of the relative Young's modulus versus relative density of the synthetic scaffolds and natural scaffold composite.....	62
--	----

LIST OF TABLES

Table 1. A list of various ceramic materials with potential as well how they are currently employed as biomaterials.....	10
Table 2. A list of biocompatible polymers and their associated uses in relation to the human body.....	12
Table 3. Physical and mechanical properties of hydrated cortical bone [81nov, Curreybook “Biomaterial Properties”], cancellous bone [80che]. (ρ = bulk density, σ = compressive strength, E = Young’s modulus).	15
Table 4. Recipes for ceramic slurries with 20 vol.% hydroxyapatite (HA), 30 vol.% HA, and 35 vol.% HA. Values are given in wt.%.	39
Table 5. Physical and mechanical properties of hydrated cortical bone [81nov], cancellous bone [80che], and natural scaffold (heated bovine cancellous bone).	47
Table 6. Physical and compressive mechanical properties of natural HA scaffolds, pure PMMA, and natural HA-PMMA composites. (ρ = bulk density, σ = compressive strength, E = Young’s modulus).	49
Table 7. Comparison of the mechanical and physical properties of cortical bone and the synthetic HA scaffolds. (ρ = bulk density, σ = compressive strength, E = Young’s modulus).	51

ACKNOWLEDGEMENTS

First and foremost, I would like to thank everybody from the Mckittrick research group and especially Prof. Joanna McKittrick for the help and support.

Thank you Katya for all those edits on my very first paper!

Thank you James for helping me keep the lab tidy and being my age!

Thank you Mike for all those edits on my other papers!

Thank you Sarah for being Sarah!

Thank you Dr. Po-Yu for the good advice and insightful comments!

Thank you Wen for the dumplings!

I would also like to thank Scott Wasko, Grace Lau, Tony Tomsia, and Adah Almutiari for their contributions, because without them this thesis would not exist.

Last, but not least, I want to thank Prof. Ratnesh Lal and Prof. Vlado Lubarda for taking the time to hear what I have to say.

ABSTRACT OF THE THESIS

Composite bone substitutes prepared by two methods

by

Hoe Y Lee

Master of Science in Materials Science and Engineering

University of California, San Diego, 2012

Professor Joanna McKittrick, Chair

A variety of ceramics and polymers exists that can be used as bone substitute materials with desirable properties such as biocompatibility and osteoconductivity. A key feature missing in these bone substitutes, or scaffolds, is the ability to bear loads. This work explored two methods for solving this problem. The first used cancellous bone taken from bovine femoral bone to create a natural scaffold through a heat treating

process that eliminated the organic components and sintered the bone minerals, known as hydroxyapatite, together. The strength and Young's modulus of the natural scaffold were greatly improved after polymer infiltration with polymethylmethacrylate. Unfortunately, compression testing revealed that there was not a good interfacial bond between the mineral and polymer phases. The second method employed a freeze-casting technique to create synthetic hydroxyapatite scaffolds that have an aligned lamellar microstructure. By varying the amount of hydroxyapatite in the initial slurry mixture and the cooling rate, synthetic scaffolds with a range of porosities and strengths was produced. The highest solid loading and fastest cooling rate produced a scaffold with a strength and modulus approaching that of cortical bone. Further study is required to produce a two phase composite that is chemically bonded together for optimal performance. The synthetic scaffolds, with their tunable mechanical properties and ease of fabrication, make them a promising material for a load-bearing bone substitute.

INTRODUCTION

Bone is an incredible multi-functional organ system. It serves as a calcium bank, storing the majority of calcium found within the human body. Housed within the long bones is marrow that produces red blood cells vital for life. In addition, bones serve in multiple structural roles where they provide muscles with anchor points necessary for locomotion and form a tough shield around vital organs such as the brain, the heart, and the lungs. As both a structural and protective system, bones must be very tough natural materials; but as tough as they are, disease and/or trauma can leave bone unable to heal itself. Bone grafts and/or bone substitutes are used to augment the healing process as well as to fill the voids or segmental defects in bone fractures. Surgical procedure is required to transplant the bone graft material, whether it is autogenous bone, allogeneous bone, xenogenic ceramics, and select synthetic materials, into and/or around the bone tissue. In 2005, approximately 500,000 procedures required a bone graft or bone substitute [1] with this occurrence expected to continually rise as healthcare costs increase. Currently, majority of the research on bone substitute materials is done in academia.

Bone grafts and/or bone substitutes are necessary for filling voids or segmental defects or as an augmentation to healing fractures. When bone fractures, the bones must be aligned properly and mated closely together in order to heal properly. When this is not possible through natural means, the fracture must be immobilized through internal fixation or external fixation and supplemented by bone graft materials should the situation require it. Bone alignment and stability are absolutely essential for bone to heal correctly. Figure 1 illustrates the effects of a poorly stabilized bone fracture. Incorrect

placement of the lag screws and bone fragment misalignment led to a non-union of the bone eight months after the initial surgery [1]. The bone fragment surfaces were unable to mate together successfully and heal as desired.



Figure 1. Radiographs showing the effects of unstable internal fixation. On the left is a radiograph taken postoperatively and on the right is another taken 8 months after the initial surgery [1].

The images in Figure 2 give some examples of how some injuries have been treated. On the left is a titanium plate that has been implanted into a human skull after surgery left the original bone non-viable. The image on the right is of a fractured tibia that required

internal fixation for the bone to heal.

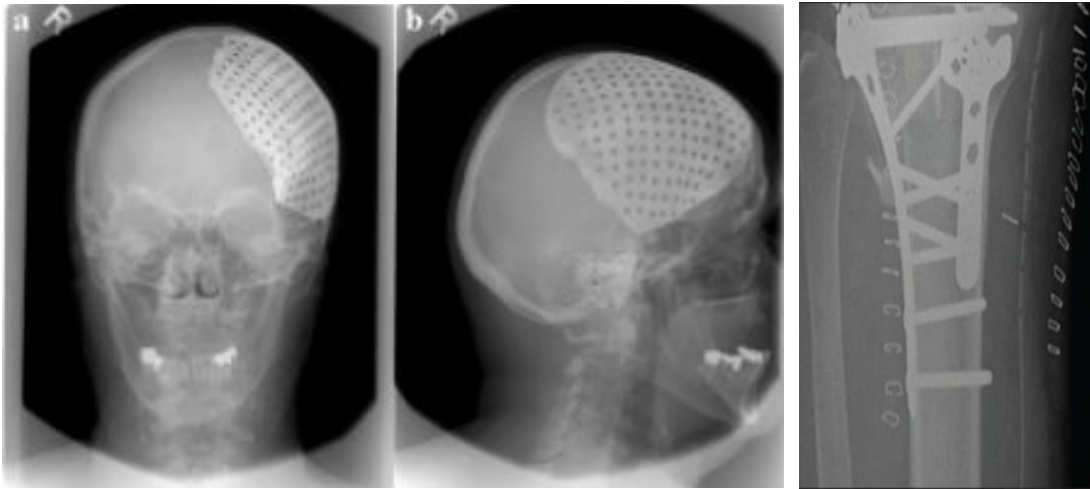


Figure 2. The x-ray radiographs of the skull on the left show an example of a titanium skull implant used after a decompression surgery [3]. The x-ray image on the far right is of a fractured tibia that required internal fixation using a combination of screws and plates [4].

Autografts harvested from a patient's own body, are considered the "gold standard" of bone grafts due to its high success rates [5,6]. Since the tissue source is from the patient's own body, there is no risk of graft rejection. The harvested bone is naturally seeded with osteoblasts (bone-forming cells), osteocytes (mature bone cells), osteoclasts (bone resorbers), and osteoprogenitor cells (cells that will differentiate to become osteoblasts) and a variety of chemical factors such as bone morphogenic protein that stimulate bone growth and remodeling [7]. Autogenous bone is sourced from cortical or cancellous bone typically harvested from the iliac crest, though the radius and tibia can also serve as donor sites [6,9,10]. Figure 3 points out the locations of the various donor sites.

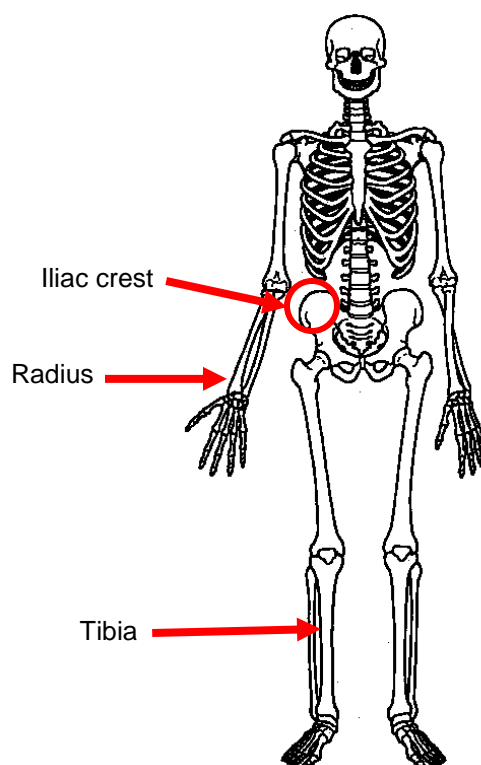


Figure 3. Anatomical locations of autograft harvest sites [11]. Bone can be taken from the iliac crest located on the pelvis, the tibia in the leg, or the radius located in the forearm.

Cancellous grafts require bone tissue ingrowth in order to develop strength over time.

Their high porosity allows new bone tissue and vasculature to rapidly penetrate the implant, but at a cost to strength. In this respect cortical bone possesses an advantage; although cortical grafts can lose up to a third of their strength due to bone remodeling, they are able to provide immediate structural support, a trait that cancellous grafts lack [12]. Autografts are not without some disadvantages. Most notably, autogenous bone is very limited in supply with just a few areas in the body that they can be harvested from. The patient's health is also a critical factor in determining autograft as a viable option. In

addition, while morbidity rates are relatively low, patients may experience pain or infection associated with autograft bone extraction [13-16].

Allograft tissue taken from a donor body is a close alternative to autografts. Allogeneic bone is sourced from bone banks that prepare them from large segments or even whole bones of donors. Unlike autogenous bone, there is no limit to the quantity or size of bone desired. Allogeneic bone grafts can be cortical or cancellous bone and also have the same advantages and disadvantages that autogenous bone has. Allogeneic bone can also be demineralized to strip the bone of all inorganics, leaving a collagen matrix known as demineralized bone matrix (DBM). Tiedeman et. al. found DBM, when combined with bone marrow, to be comparable with iliac crest autogenic bone in its success rate [17]. Grafton, a commercial DBM material available in a variety of form factors (Figure 4), has proven to be a suitable alternative to autogenic bone in several studies [18-21].



Figure 4. Grafton DBM is available in various shapes and sizes (manufacturer image).

Peterson et. al. compared the performance of three commercially available DBM preparations (Grafton Putty, DBX Putty, and AlloMatrix Putty) by testing them in rat

spinal fusion models. At eight weeks, the Grafton grafted spines were 100% successful, while DBX only saw 50% and 0% for AlloMatrix [22]. Gao et. al. were able to repair an osteochondral defect located in rabbit femur up to 95% of the original depth in just 12 weeks by seeding DBM with bone marrow derived mesenchymal stem cells [23]. These two case studies are good examples of how flexible DBM can be in its use as a bone substitute. However, since DBM is a soft collagen matrix it can only be used to fill stable bone defects or as a supplement to autogenous bone.

Allogeneic bone substitutes have some serious risks associated with their use. Since it is foreign tissue, a significant amount of time and money is invested in proper extraction, sterilization, storage, and transportation procedures for harvested tissue [24]. The most important step, sterilization, carries serious consequences if carried out improperly. The bone has the potential to trigger a serious immune response or in the worst case scenario act as a vector for disease. There have been documented cases of allograft tissue transferring HIV or parasitic infections into allograft recipients due to improper sanitization prior to use [25]. Despite their advantage as a human tissue, allografts have the potential for very serious adverse effects.

A safer alternative to allografts are ceramic scaffolds fabricated from xenogenic or synthetic materials. A large number of ceramic scaffolds are based upon calcium phosphate and its derivatives. They are highly compatible with natural bone tissue since natural bone contains hydroxyapatite (HA) minerals ($\text{Ca}_5(\text{PO}_4)_3(\text{OH})$), a form of calcium phosphate where 4-6% of the phosphate groups have been replaced by carbonate [26].

Currently, xenographic bone substitutes are produced from bovine bone and coral skeletons. The bovine bone is deproteinized to remove all organic material, leaving a

scaffold that is purely HA. Bio-Oss is a commercial product of this nature that is available in a range of granule sizes. In a ten year follow-up of maxillary sinus augmentation, Sartori et. al. found that Bio-Oss stimulated growth of lamellar bone and that it was being resorbed and replaced by natural bone [27]. In Figure 5 Bio-Oss® is compared with human cancellous bone and shown to have very similar microstructures.

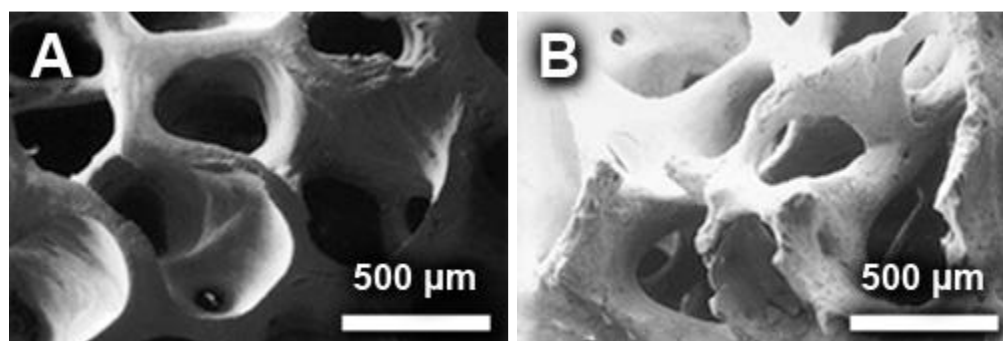


Figure 5. Microstructure comparison of Bio-Oss® (left) and human cancellous bone (right) (SEM 50x). The Bio-Oss® produced from bovine bone has features (i.e. porosity) that are very similar to human bone (Manufacturer images).

Another interesting material sourced from nature is coralline calcium carbonate, CaCO_3 . In a 5-year study of Biocoral® a commercial coralline bone substitute, Yukna et. al. found that bone defects treated with Biocoral® healed favorably with long term clinical benefits [28]. Like Bio-Oss®, Biocoral® has a porous microstructure that mimics human cancellous bone (Figure 6).

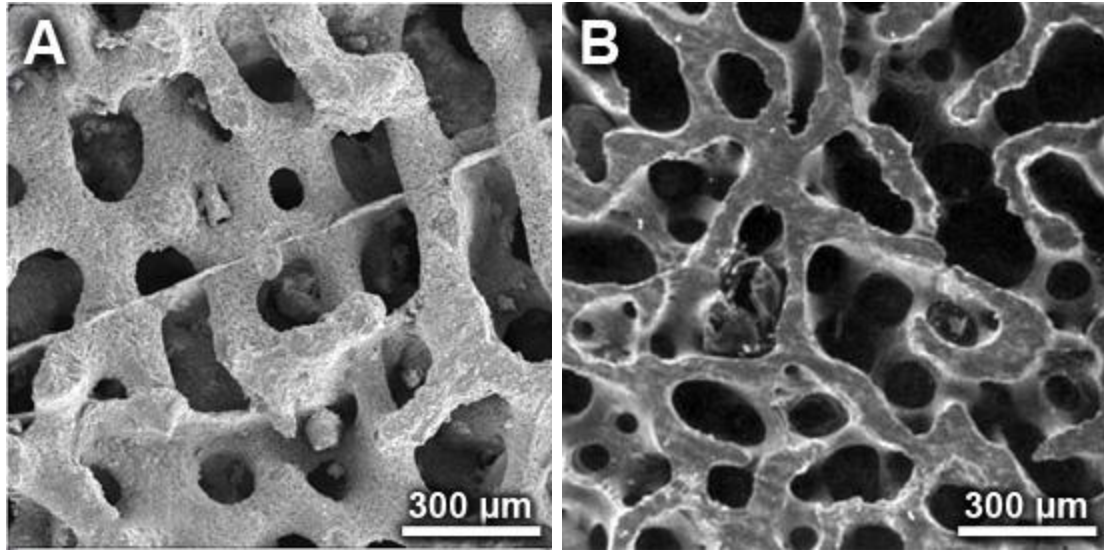


Figure 6. Microstructure comparison of Biocoral® (50% porosity) (a) and human cancellous bone (b). Like Bio-Oss®, Biocoral® possesses microstructural features that mimic those of human cancellous bone.

Unlike the allogeneic bone, the xenogenic bone substitutes are only produced in small form factors such as pellets and granules. This limits their use to filling in small voids and defects, so they find popular use in facial reconstruction and dentistry. They also have high porosity which leads to low strength compared to natural cortical bone (~100 MPa), but higher than cancellous bone (~2-6 MPa).

Ceramic bone substitutes come in a variety of compounds and morphologies. Some of these materials include alumina (Al_2O_3), zirconia (ZrO_2), and titania (TiO_2). The most popular of these are hydroxyapatite (HA), $\text{C}_{10}(\text{PO}_4)_6(\text{OH})_2$, and tricalcium phosphate, $\text{Ca}_3(\text{PO}_4)_2$. HA is the mineral component found in bone which makes it naturally biocompatible and gives it potential to be osteoconductive wherein bone forming cells will readily migrate into the implant [29,30n]. Crystalline HA has been shown to have a slow resorption rate of 1-2 % per year [34]. Johnson et. al. found that in

a 24 week trial of HA and tricalcium phosphate, only the tricalcium phosphate showed any signs of biodegradation [31]. Some synthetically derived and commercially available HA and calcium phosphate materials include Bioresorb®, Chronos®, Ceros®, and Cerasorb®. Figure 7 shows the development of bone growth after a giant cell tumor was excised from the distal end of a tibia and subsequently filled with pure HA granules (Figure 7(b)) [32]. Injectable cements have also been developed. These are calcium phosphate based cements that harden non-exothermically *in vivo* after injection. Materials for these cements include dicalcium phosphate dehydrate and calcium deficient hydroxyapatite. In trials using rabbits, Ohura showed that an injectable calcium phosphate cement resorbed completely and was replaced by bone quickly [33]. Both the solid and injectable materials are brittle by nature; strong in compression, but weak in tension and shear. This limits ceramic bone substitutes to small form factors and non-load bearing applications such as void and defect filling and as an autograft extender.

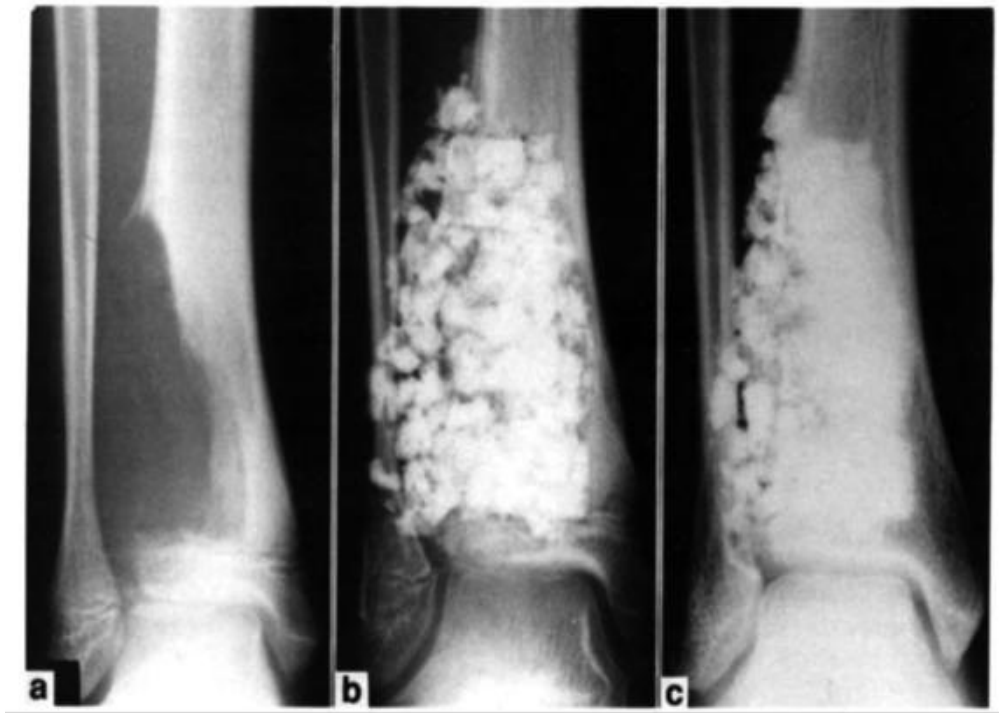


Figure 7. Series of radiographs showing bone development after removal of a giant cell tumor at the distal end of the tibia. a) Before surgery. b) Immediately after surgery. Visible are the hydroxyapatite granules packed into the void left by tumor removal. c) 3 years after surgery [32].

Table 1. A list of various ceramic materials with potential as well how they are currently employed as biomaterials.

Ceramic	Usage	Ref.
Tricalcium phosphate	Bone graft expander, cement	34
Hydroxyapatite	Bone graft expander, cement	34
Calcium sulfate ?	Bone filler	34
Aluminum oxide	Bone graft expander	34
Titanium oxide	Bone graft expander, implant coating	35
Zirconium oxide	Coating, joint replacement	36

In addition to ceramics, various polymers are being explored as bone scaffold materials. Synthetic polymers can be produced with consistent mechanical properties in a variety of morphologies. Through fabrication techniques such as salt leaching [37] or phase inversion [38], polymers can take on microstructures that mimic cancellous bone (Figure 8). Common polymers including polylactic acid and polymethylmethacrylate can be fabricated with impurities such as therapeutic drugs or growth factors that are released in a controlled fashion with the body [39-43].

Table 2 gives some examples of polymeric biomaterials and their corresponding medical applications.

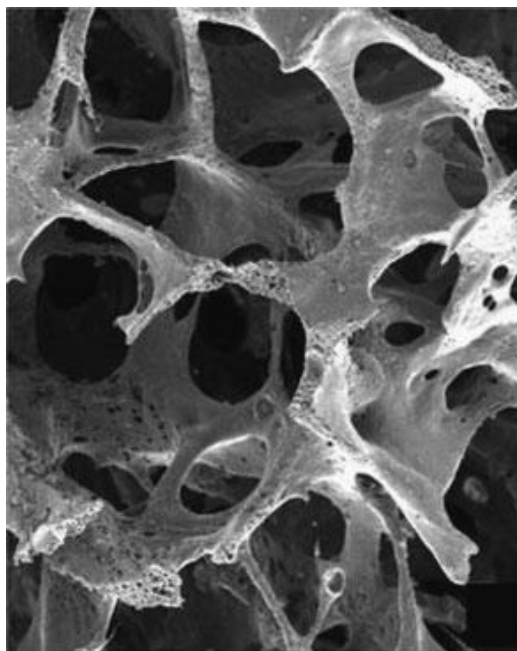


Figure 8. Poly(lactic-co-glycolic-acid) scaffold (Osteofoam™) obtained by phase inversion. [42].

Table 2. A list of biocompatible polymers and their associated uses in relation to the human body.

Polymer	Usage	Ref.
Polyethylene	Hip arthroplasty	41
Polyurethane	Abdominal aortic repair	42
Polytetrafluoroethylene	Abdominal wall repair	43
Polyacetal	Hip arthroplasty	44
Polymethylmethacrylate	Bone cement	45,46
Polyethylene terephthalate	Abdominal wall prostheses	47
Polyether-ether ketone	Bone plates and screws; hip replacement	48,49
Polysulfone	Spinal plate, fracture fixation	50
Polylactic-co-glycolic acid	Tissue scaffold	51,52,53
Polypropylene fumarate	Tissue scaffold	54
Polyaryletherketone	Bone plates and screws	48

Cortoss, a bispheno-a-glycidyl dimethacrylate resin, has been proven to be safe and effective as cement for vertebroplasty [59]. Unfortunately, polymer scaffolds are not without their drawbacks. They are not as strong as cortical bone and cannot serve in major structural roles. This weakness is compounded by the introduction of porosity introduced into many of the polymer materials. Also, if the biodegradation rate is not precisely controlled, the acids released from the scaffolds can alter the pH of the local environment, greatly affecting the activity of living tissue [60].

In summary, a variety of bone grafts and bone substitutes are available to treat different types of bony defect and fractures. As mentioned, autografts are the optimal material, but are restricted by a limited supply and donor site morbidity. Allogeneic materials are the next most desirable material. However, disease transmission is a serious concern. Xenogenic bone substitutes have just the right chemical composition and physical structure to be on par with allogeneic materials, but like allografts much time and money must be invested to process them into suitable bone scaffolds. Synthetic ceramics and polymers are advantageous in that they do not require additional surgery to procure them or carry the risk of disease transmission. Their physical and chemical characteristics can easily be tailored to specific tasks. To date, however, synthetic materials have been restricted to small form factors for use in non-load-bearing roles. A bone substitute that successfully combines high porosity with a load-bearing capability has not yet been developed. A substitute with both these characteristics would have wide reaching benefits. Patient care would be greatly enhanced through a potential reduction in healing time which in turn would lead to lower medical costs.

BACKGROUND

Developing a bone substitute requires a deep understanding of the physical, chemical, and biological nature of bone. Bone is a complex hierarchical material with structural levels that range from the macro to nano, as illustrated by Figure 9. The structure-function interplay of each hierarchical level and their relationship with the properties of whole bone is difficult to surmise. However, studying bone and its constituent sub-structures can provide insight into what may constitute a desirable bone substitute material.

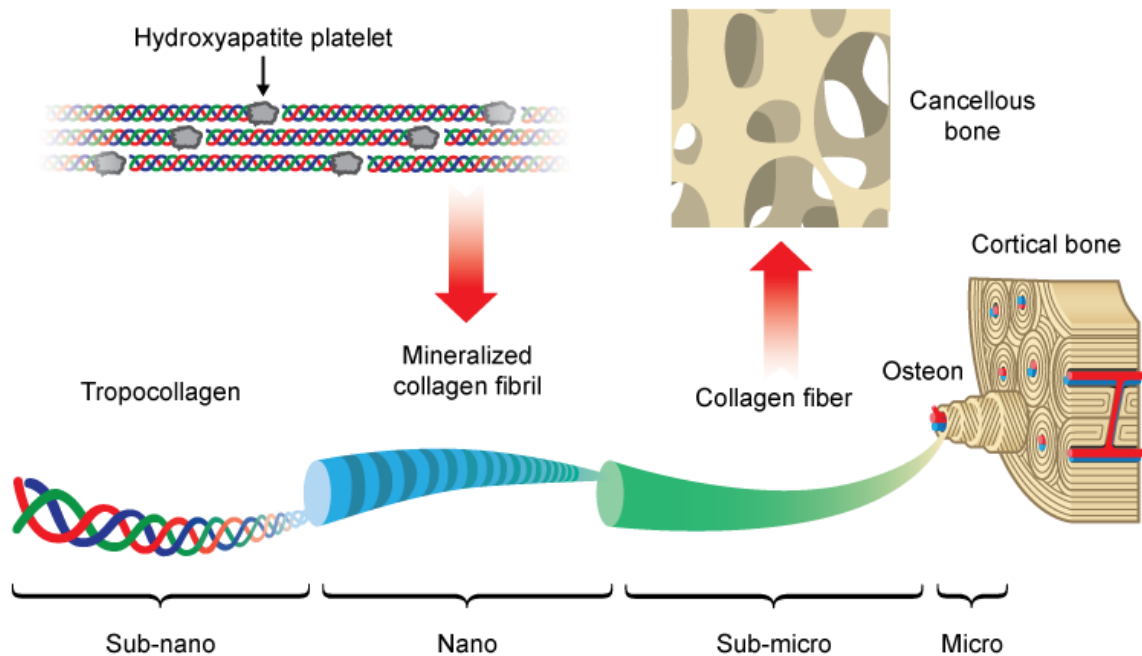


Figure 9. Hierarchical structure of bone showing the various length scales involved in building up to whole bone.

At its heart, bone is built on four principle components: hydroxyapatite (HA) minerals, type-I collagen, water, and non-collagenous proteins (NCPs). By weight bone is ~70 wt.% minerals, ~20 wt.% organics, and ~10 wt.% water [61t].

Table 3. Physical and mechanical properties of hydrated cortical bone [83], cancellous bone [82]. (ρ = bulk density, σ = compressive strength, E = Young's modulus).

	wt. % mineral	wt.% organic	wt.% water	ρ (g/cm ³)	σ (MPa)	E (GPa)
Cortical bone	65	25	10	2.0	110 – 150	18 – 22
Cancellous bone	--	--	--	0.2 – 0.5	2 – 6	0.1 – 0.3

The minerals have a plate shaped morphology with an average length and width of 50×25 nm [62]. They are remarkably thin as seen by transmission electron microscopy (Figure 10) and have a relatively uniform thickness that varies between 3 to 4 nm [64]. It is worth nothing that these crystals are the smallest crystalline biominerals that have been discovered so far [62]. It is yet unknown why the minerals are thin plates, but it has been speculated that they are formed by an octacalcium phosphate precursor which are plate-shaped by nature [65]. To date, the mechanical properties of single bone crystals have not been measured, presumably due to the extremely small size. Samandari tested single crystals of synthetic HA using nanoindentation and found them to have a Young's modulus of 150.4 GPa [66].

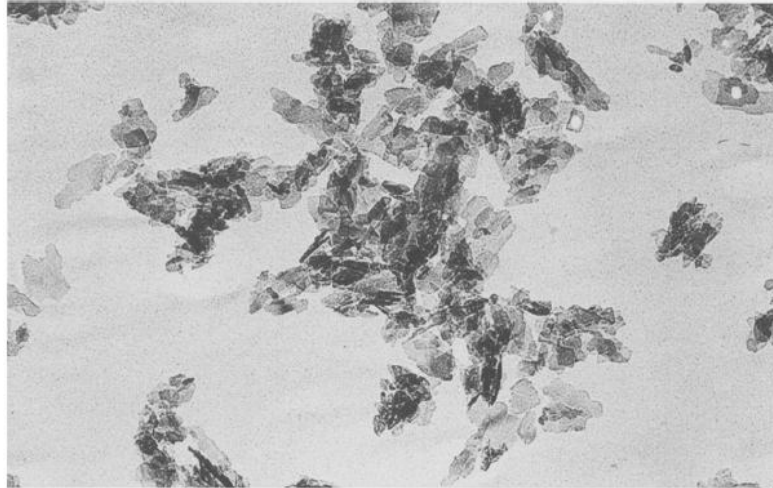


Figure 10. Transmission electron micrograph of the hydroxyapatite crystals from human bone (put scale bar) (taken from Weiner) [63].

The organic material in bone is primarily composed of type-I collagen fibrils with a small fraction being NCPs [26]. The collagen fibrils are composed of triple helix tropocollagen molecules that consist of three polypeptide chains with two identical $\alpha 1(I)$ chains and a third $\alpha 2(I)$ chain [67] that are each approximately 1000 amino acids long [68]. These molecules are approximately 1.5 nm in diameter and 300 nm in length. Bundled together, they form a fibril about 80-100 nm in diameter. Figure 11 shows a schematic illustration of how the molecules are arranged. Between molecules there is a gap of 35 nm that is typically occupied by HA crystals. Adjacent columns of molecules are offset by 67 nm along the long axis, an arrangement first proposed by Hodge and Petruska [69]. Under transmission electron microscopy (TEM), this staggered arrangement of HA containing gaps shows up as a pattern of periodic bands (Figure 12).

In addition to the minerals and collagen, water has a significant effect on the mechanical behavior of bone. Nyman et. al. showed that dehydration of bone tissue leads

to an increase in Young's modulus and strength, whereas the strain to failure drops [70]. This is not a surprising find, knowing that water is found throughout the collagen matrix; it fills space within the collagen fibrils, between the fibrils, in the gaps, and in between the molecules [71]. Dispersed throughout the collagen matrix are the NCPs. As of yet, it is unclear whether NCPs serve a structural role, but it is thought that they may serve to stimulate bone growth and remodeling [72,73,74]. Discounting NCPs, the three major elements described previously are the building blocks upon which bony tissue is formed.

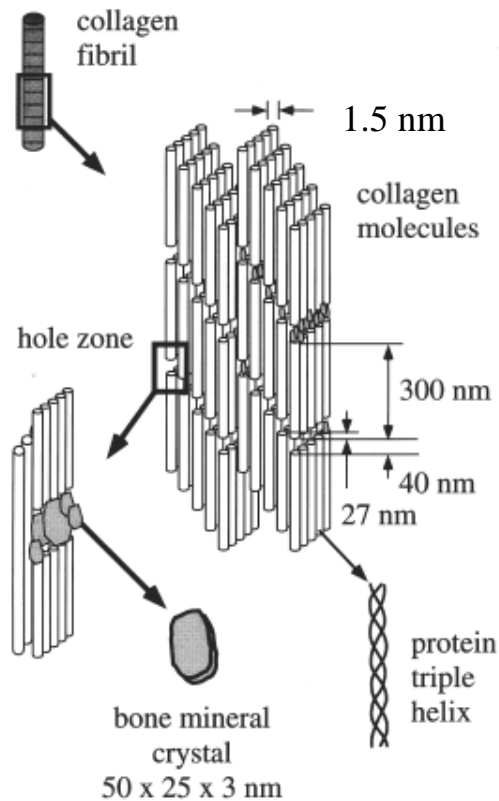


Figure 11. A schematic illustration of the nanostructure of collagen. (taken from Rho) [64].

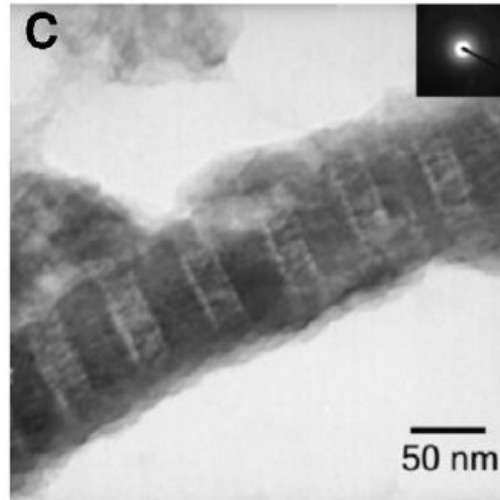


Figure 12. TEM brightfield image of an isolated collagen fibril showing the characteristic banding pattern of type-I collagen. The inset image (top right) is a selected area electron diffraction (SAED) pattern. The pattern is diffuse, suggesting that the electron dense phase is amorphous CaP. The sample was not stained (taken from Olszta) [26].

A step up in the structural hierarchy introduces fibrillar bundles. Weiner defines collagen fibril arrays as one of four arrangements illustrated in Figure 13: parallel arrays, woven fibers, plywood-like lamellar structures, and radial arrays [65].

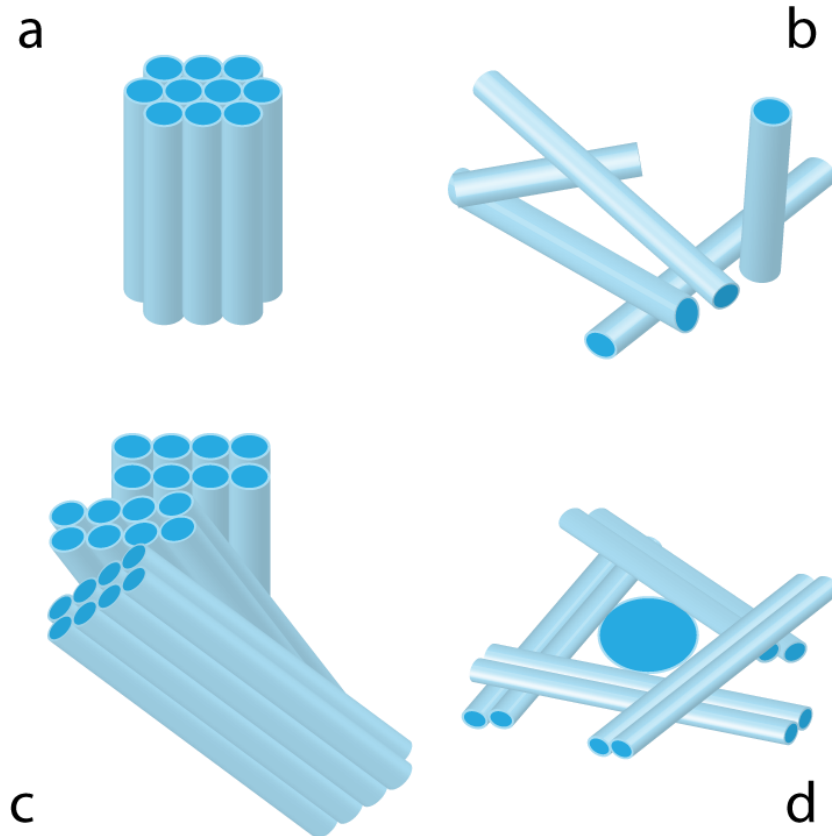


Figure 13. Schematic illustrations of the four types of collagen fibril arrangements. a) Array of parallel fibrils. b) Woven fiber structure. c) Plywood-like structure present in lamellar bone. d) Radial fibril arrays (adapted from Weinan).

Arrays of parallel fibrils can be found in parallel fibered bone. In this arrangement, the collagen fibrils are parallel to each other along their long axes. Microhardness testing of parallel fibered bone has shown that it is an anisotropic material with a hardness value of $.598 \pm 0.058$ GPa in the longitudinal direction (parallel with the long axis) and 72 ± 9.0 GPa in the transverse direction (orthogonal to the long axis) [75].

The second fibril arrangement (Figure 13(b)) is the woven fiber structure. Unlike the parallel fibers in the previous example, the fibrils in woven bone are not arranged neatly. Figure 14(d) shows a scanning electron microscope image of the woven fibril

arrangement found in human fetal bone [76]. Su et. al. found that woven bone from human fetal femurs contained plate shaped HA minerals that increased in length (18.1 nm to 31.6 nm) and width (11.5 nm to 19.2 nm) as age of the fetus increased (from 16 to 26 weeks) [76]. The image shows that the woven fibrils are not well ordered and are only loosely packed compared to the parallel fibrils in Figure 14(c). Important to note, though, is that the woven fibrils of woven bone are formed rapidly and quickly replaced by other forms of bone. It is the first type of bone to form when injury or disease stimulates the growth and repair of bony tissue.

The third fibril arrangement (Figure 13(c)) is the plywood-like structure. In this arrangement collagen fibrils are arranged into discrete layers. The fibrils in each layer run parallel with each other and the fibril or fiber orientation of each layer is different. Weiner found that that in rat lamellar bone that each layer was rotated 30° with respect to the previous layer in a rotated plywood structure [77]. This is very similar to modern laminated composites where the fibers of each layer are at different orientations to optimize strength or stiffness. Interestingly, the mechanical properties of this type of arrangement in baboon tibia revealed that the mechanical properties were greatest in the direction of the long axis of the bone and weakest in the direction orthogonal to that [65].

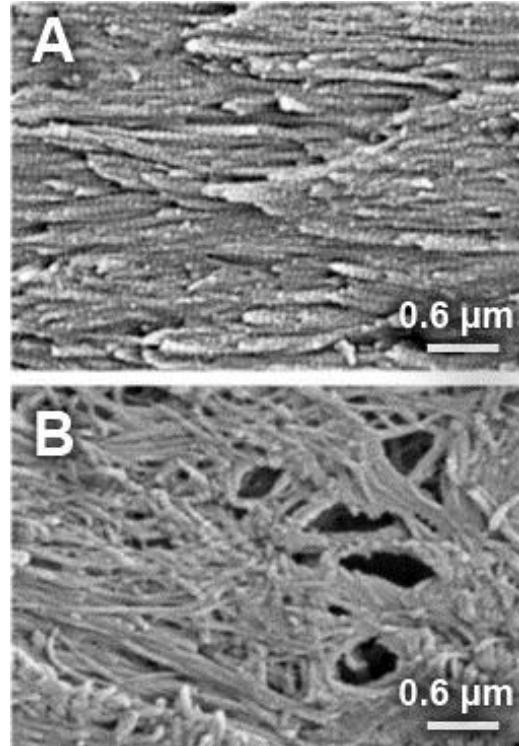


Figure 14. Scanning electron images of human fetal bone comparing parallel (a) fibrils to (b) woven fibrils. The fibrils in the parallel arrangement are densely packed and well ordered, whereas the fibrils in the woven arrangement are unorganized and loosely packed with visibly empty pockets (taken from Su) [74].

The fourth and final type of fibril arrangement is the radial array Figure 13(d).

This pattern is most commonly found dentin, the material which makes up the inner layer of teeth [65]. The fibril layers are found parallel to the surface where dentin is formed and grows. The HA crystals in these fibrils have little to no ordering. Wang found that the crystals show some directional alignment with respect to individual fibrils that does not extend to neighboring fibrils [78].

These various fibril arrangements at the sub-micron scale give rise to two main types of osseous tissue, dense cortical bone (2.0 gm/cm^3) and porous cancellous bone ($\ll 2.0 \text{ gm/cm}^3$). Their distinguishing feature is not purely based on density, as will be

discussed. Cortical bone can be distinguished by a system of cylindrical lamellar structures called osteons, also known as Haversian systems. Osteons are composed of lamellar mineralized collagen fibers formed into concentric circles around a central vascular channel (Haversian canal) that houses the bone's blood supply. The layers have a rotated plywood arrangement (Figure 15(b)) and decreasing in thickness moving from the inner radius to the outer radius [65]. In between each lamella are lacunae spaces (Figure 15(a)) that each house a single osteocyte, a bone cell responsible for remodeling bony tissue. Hannah used micro-CT to analyze the volume of ~10,000 lacunae averaged over 11 osteons and found that there was a bimodal distribution of lacuna space volumes at $200\text{ }\mu\text{m}^3$ and $330\text{ }\mu\text{m}^3$ [79]. Each lacuna space is connected other lacuna spaces by a network of tiny canals known as canaliculi (Figure 15(a)). Volkmann's canals connect the Haversian canals to each other, forming a vascular network that penetrates throughout the bone Figure 15(b). In between individual osteons are interstitial lamellae, leftovers from older osteons that have been partially resorbed. Rho et. al. performed a series of nanoindentation tests on osteonal lamellae and found that hardness and Young's modulus decreased from the innermost lamellae closest to the Haversian canal and moving outward. The results of his testing plotted on Figure 16 [80].

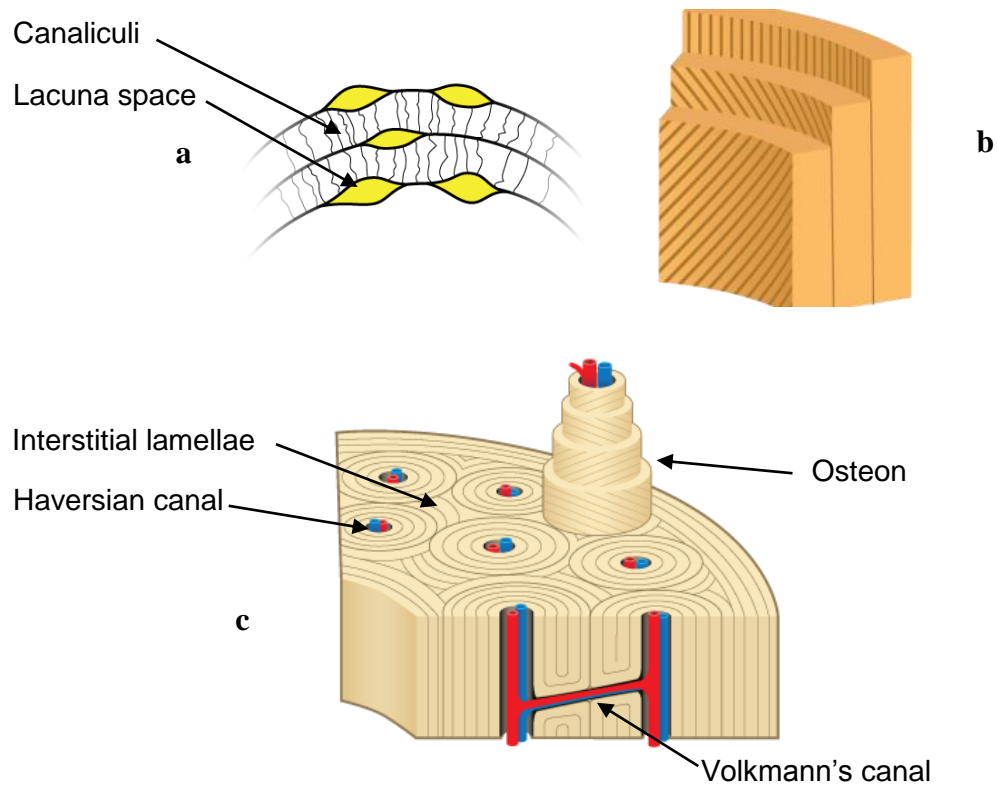
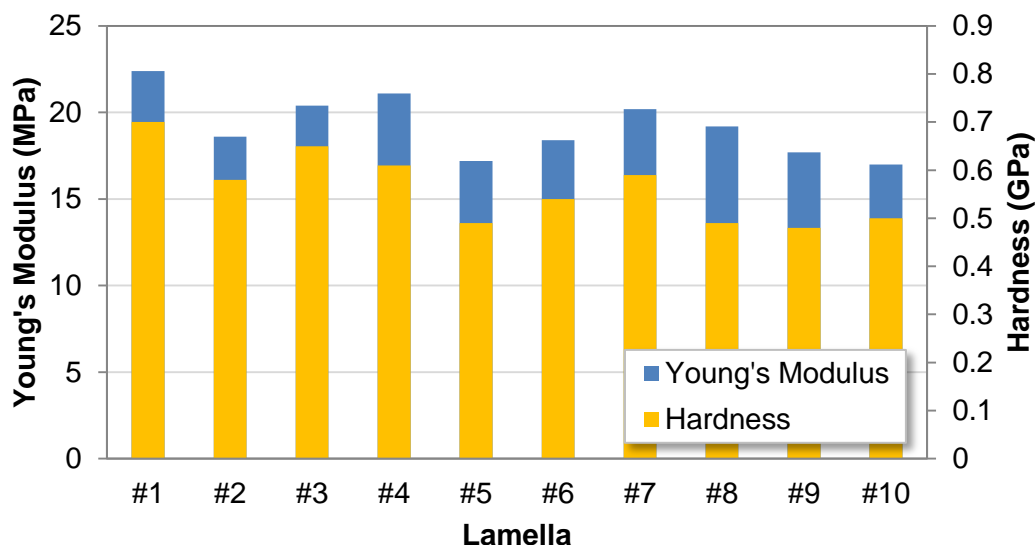


Figure 15. a) Diagram of the lacunae spaces (yellow) connected by a network of channels known as canaliculi. b) A partial section of an osteon. The lines indicate the fiber orientation of each lamella. c) The protruding osteon displays the multiple layers that it is composed of and is shown surrounded by other osteons within the context of cortical bone.

Figure 16. Young's modulus and hardness as a function of the lamella in an osteon. Lamellae #1 is nearest to the Haversian canal and #10 is furthest. Both mechanical properties decrease moving outward from the center of the osteon (adapted from Rho) [80].



Croft et. al. found that the degree of mineralization in the osteonal lamellae decreased with distance away from the central Haversian canal [81]. These findings correlate well with the nanoindentation testing performed by Rho. In its natural hydrated state, cortical bone taken from a bovine femur had a compressive strength of 12.7 MPa and an Young's modulus of 0.67 GPa [82]. Cancellous bone differs from this in both micro- and macrostructural properties.

Cancellous bone is younger, on average, than the cortical bone that surrounds it.. Cancellous bone is more metabolically active and is remodeled much more often than cortical bone [80]. At the macro scale, this translates to cortical bone that is denser, older, and more mineralized than cancellous bone. Unlike cortical bone, cancellous bone contains flat lamellae rather than cylindrical osteons [83] that are the basis for trabeculae, the small beam, rod, or strut elements that make up cancellous bone. These are

constructed together into a lattice that has the appearance of highly porous open cell foam (Figure 9) with high surface area and low density ($0.2 - 0.5 \text{ g/cm}^3$). Bone growth depends on the loads imposed on it. Its density and morphology are shaped by the magnitude and direction of the applied load. In regions of low stress, open cell rod-like structures develop (Figure 17(a)), whereas in regions of high stress denser plate-like structures appear (Figure 17(b)). Intermediate regions exhibit both structures, as seen in Figure 17(c). Morgan et. al. found that the Young's modulus of cancellous bone was site-specific, depending on anatomical location. At a given density, the modulus could change up to 50% when comparing bone from the vertebra and femoral trochanter [84].

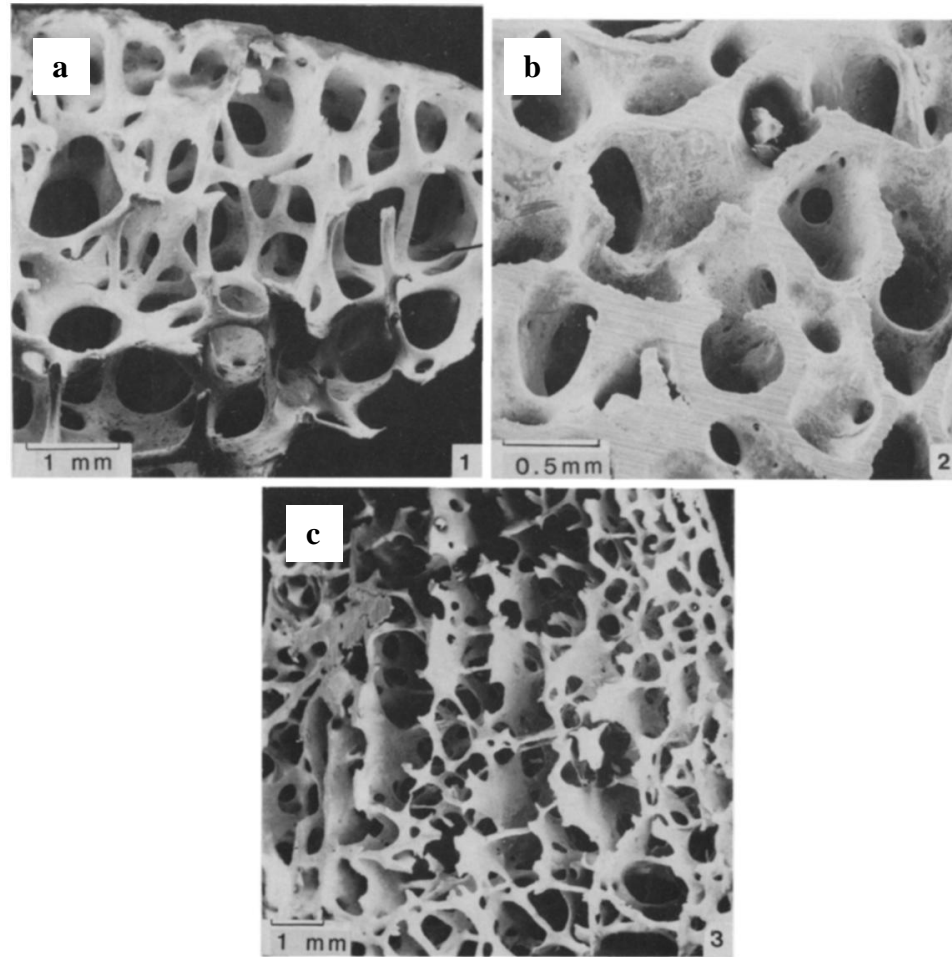


Figure 17. SEM images of cancellous bone taken from a femoral head (a, b) and the femoral condyle (c). These images illustrate the various morphologies of cancellous bone: a) rods, b) plates, c) plate-like columnar (taken from Gibson) [85].

Desirable Implant Characteristics

Bone is a uniquely complex composite relying on the interplay of each hierarchical level to achieve its strength, toughness and low density. When synthesizing bioinspired materials for use as a bone implant/substitute, these and several other important factors must be taken into consideration:

- Biocompatibility
- Biodegradability/resorbability
- Osteoconductivity
- Osteoinductivity
- Interconnected porosity
- Proper stiffness and strength

All biomaterials must be biocompatible to avoid a chronic immune response by the host.

In some cases biodegradability or bioresorbability is desirable so that natural tissues eventually grow into and replace the implant, restoring full function back to the host. The materials for bone implants should be osteoconductive, so that cells such as osteoprogenitor cells are attracted to and populate the interior of the implant. The surface should also stimulate osteoprogenitor cells to differentiate into bone growing osteoblasts. Bone morphogenetic proteins (BMPs) are a family of growth factors can produce this effect in the osteoprogenitor cells [87]. A porous implant is required so that cells have a space to move into and grow in. Implant porosity has a direct effect on osteogenesis and integration with natural bone [88, 89]. The pores must be interconnected with an interconnection size of at least 50 μm which is needed to promote bone ingrowth [90]. Hulbert et al. determined that a minimum pore size of at least 100 μm was required for significant ingrowth of bone into an implant [91]. More recent studies by Chang et al.,

have shown that 50 μm pores in a HA block showed evidence of osteon like structures at 8 weeks after implantation into a rabbit [92].

Beyond biocompatibility, the mechanical stresses experienced by bone can greatly affect its growth and remodeling. A stiffness mismatch between the implant and bone, wherein the implant is of higher stiffness, may cause a reduction in bone mass surrounding the implant over time. This well-studied phenomenon, known as stress shielding, is a result of the growth and remodeling of bone in response to external loading [93-97]. A clear example of this can be seen in Figure 18 which compares a postoperative radiograph taken of a hip replacement with another taken after a period of two years; at the two year mark, there is an appreciable loss in bone mass in the femur near the femoral head. Producing a successful bone substitutes requires a material that can blend in with natural bone.

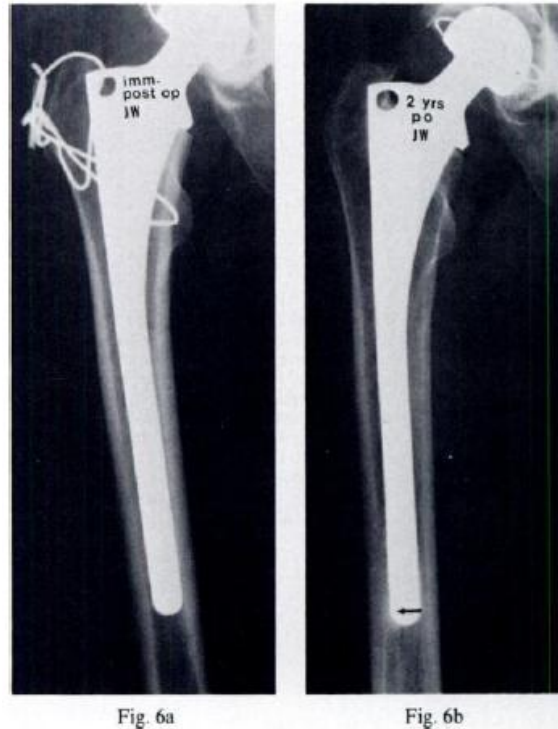


Figure 18. Radiographs of a 51-year-old woman's hip implants illustrating the effects of stress shielding. (a) Postoperative (b) Taken 2 years after implantation. There is a marked loss in bone density near the femoral head. (taken from Engh) [98].

Introduction to Freeze-casting

A new method developed to produce highly oriented, microstructures with varying porosity is freeze-casting. Freeze casting of biocompatible ceramics, primarily using HA, has been explored by a number of research groups for bone tissue engineering applications [99-111]. Freeze-casting is a physical process in which an aqueous slurry, typically composed of a solid phase (i.e. ceramic powder) and a fugitive liquid carrier (e.g. water), is directionally frozen in a mold, then sublimated to remove the frozen liquid phase and sintered to densify the porous ceramics [112]. The process is an elegant method for developing bone scaffolds where physical and mechanical properties are

intricately controlled by relatively simple modification to slurry formulations or cooling rates.

Wegst et. al. took theory previously used to describe unidirectional solidification of eutectic alloys and applied it to freeze-casting to develop a better understanding of the process. During solidification where ice crystals are formed, particle trapping is required to produce desired microstructures. Particle trapping depends on two main parameters: the free energy of the system and velocity of the growth front. First, the free energy of the system ($\Delta\sigma_0$) must be negative

$$\Delta\sigma_0 = \sigma_{ps} - (\sigma_{pl} + \sigma_{sl}) < 0, \quad (1)$$

where σ_{ps} , σ_{pl} and σ_{sl} are the surface energies between particle and solid, particle and liquid, and solid and liquid, respectively [113]. Second, the velocity of the growth front (v) must be greater than the critical velocity (v_{cr}) determined by a balance of the attractive force (F_η) and repulsive force (F_R) acting on the particle

$$F_h = \frac{6phnr^2}{d} \quad (2)$$

$$F_R = 2prDS_o \left(\frac{a_o}{d} \right) \quad (3)$$

$$n_{cr} = \frac{DS_o a_o}{3hr} \quad (4)$$

where η is the dynamic viscosity of the liquid, r is the radius of the particle, a_0 is distance between the molecules in the liquid layer, and d is the thickness of the liquid layer between the particle and the solid-liquid interface [113]. If the velocity of the freezing front is lower than v_{cr} , the particles in suspension will be rejected and pushed above the growth plane; if the velocity is faster, particle trapping will occur. Figure 19 shows a graphical representation of a particle near the liquid-solid interface during freeze-casting [113]. Particle trapping culminates in a lamellar structure characteristic of freeze-casted systems based on water as a fugitive liquid. From solidification theory, the interlamellar spacing (λ) of directionally solidified eutectic systems is shown to be inversely proportional to the thermal gradient (Figure 20) [114].

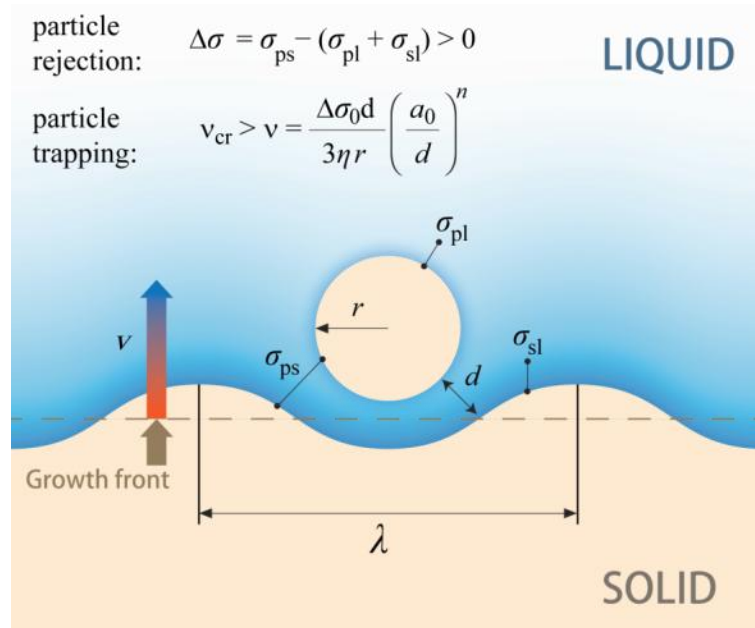


Figure 19. Schematic of particle–freezing-front interactions. (Adapted from Wegst) [113].

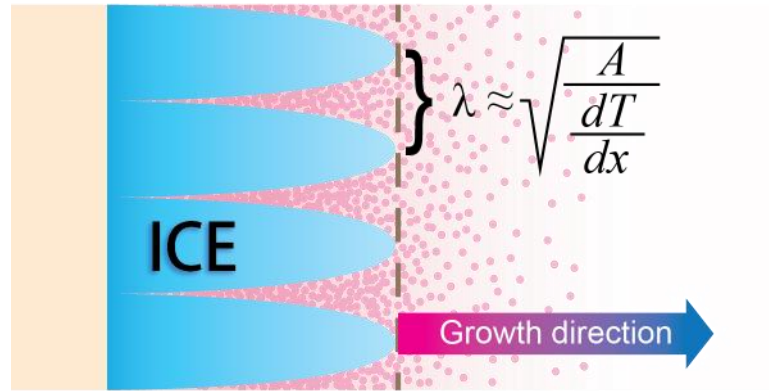


Figure 20. Illustration showing ice growth during freeze-casting. Through control of the thermal gradient, the interlamellar spacing (λ) can be modified. $A = \text{constant}$.

As the thermal gradient increases, the velocity of the growth front increases while the interlamellar spacing decreases. This was demonstrated experimentally by Deville et al. [115] where the interlamellar spacing was empirically found to be

$$\lambda \sim v^{-n} \quad (5)$$

where λ is the interlamellar spacing, v is the freezing front velocity, and the constant n depends on the ceramic particle size. Knowledge of how these parameters relate to each other allows for the fine tuning of freeze-cast structures.

The initial fugitive liquid phase can have a pronounced effect on the microstructure of freeze-cast ceramics. For instance, using water as a solvent will produce a lamellar microstructure. Water typically solidifies as hexagonal ice crystals that grow 10^2 - 10^3 times faster along the crystallographic a direction than it does in the c direction [116]. This is aided by the ceramic particles that are trapped between growing

ice crystals which further prevent growth in the c direction. Additives can be used to modify the solidification behavior of the aqueous phase and produce very different microstructures. Figure 21 gives an example of how the microstructure can vary through additive addition. In Figure 21(a) is HA freeze-cast in pure water showing the typical lamellar structure that is generated by ice crystals. Figure 21(b) and (c) show wildly different structures after the addition of glycerol or dioxane.

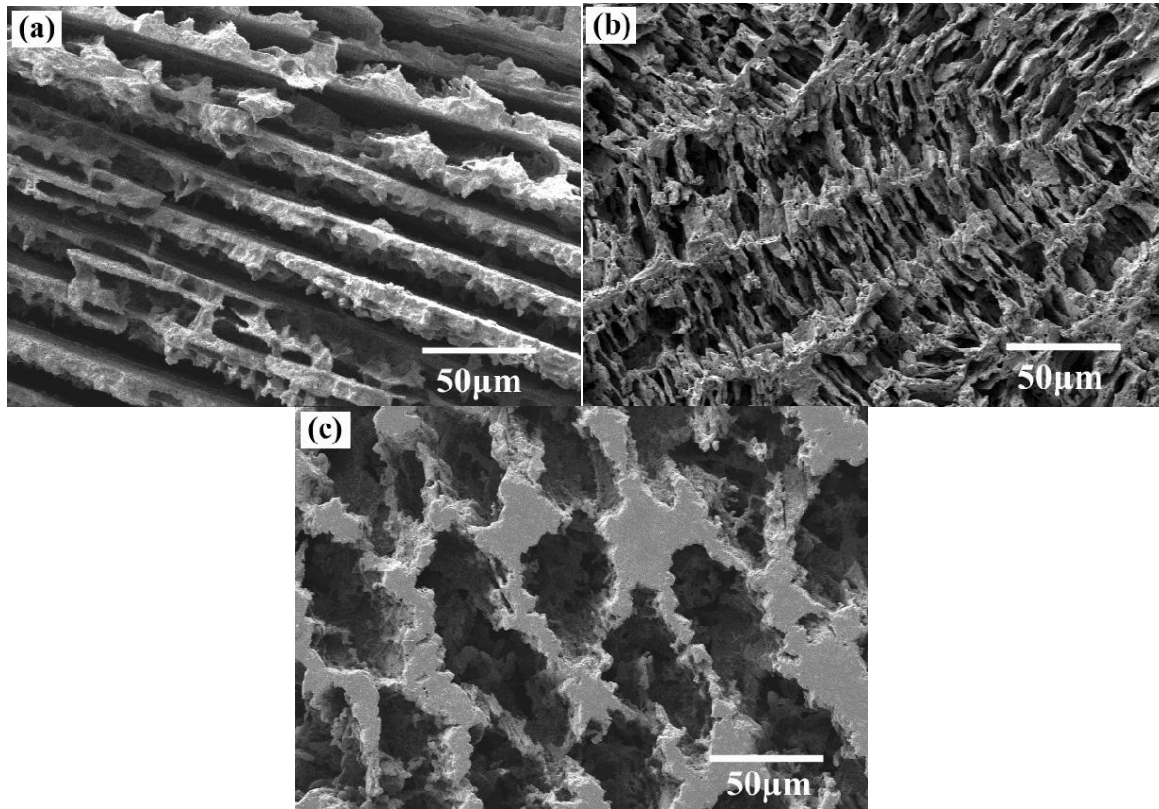


Figure 21. Effects of additive addition to the microstructure of freeze-cast ceramics. a) Water, b) water + 20 wt% glycerol, and c) water + 60 wt% dioxane (taken from Fu) [102].

Figure 23 and Figure 24 show the effects of these additives on the freeze cast microstructures at increasing concentrations. Both additives disrupt the normal crystallization of ice crystals and result in the rectangular (glycerol) or spheroidal

(dioxane) microstructures. Glycerol binds to water molecules and creates amorphous regions of ice [116]. Figure 22 shows how gelatin addition to a HA slurry was found to create spherical interconnected pores that decreased in size as gelatin concentration was increased [117]. Addition of gelatin caused the ceramic particles to aggregate and stick to each other, making the slurry more viscous and blocking the water from solidifying as it does without additives (Figure 22).

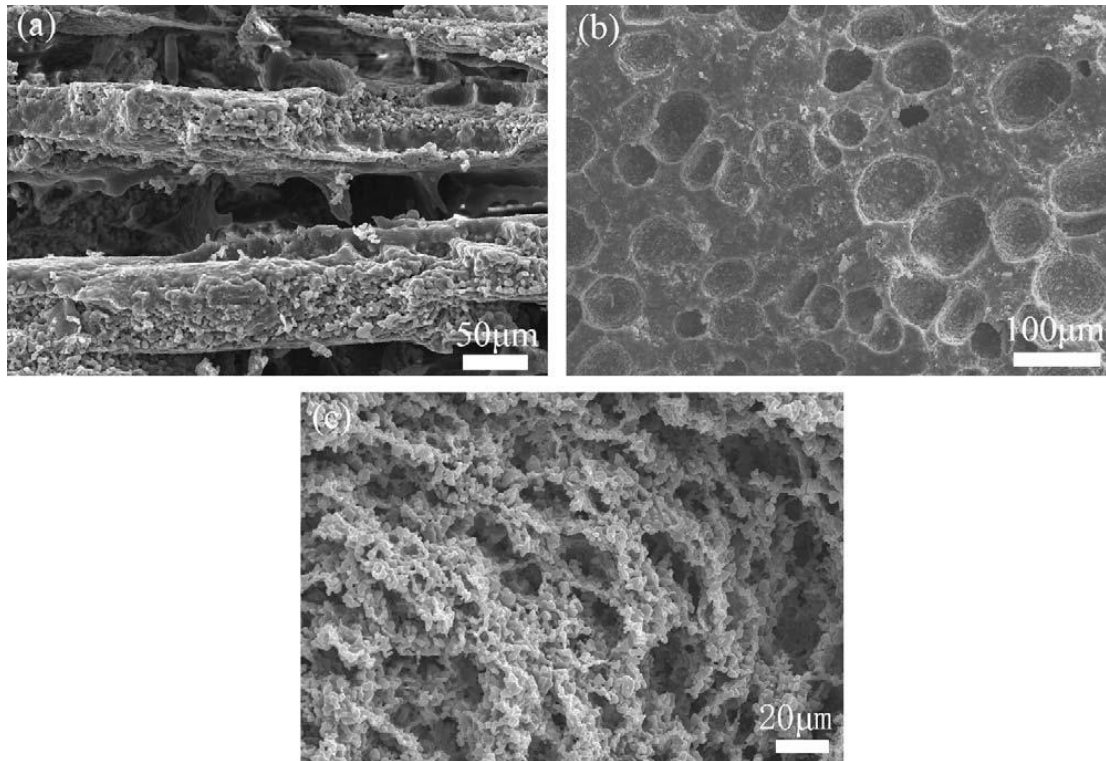


Figure 22. Microstructural evolution of freeze-cast HA on addition of different concentrations of gelatin. (a) 0 wt.%, (b) 2 wt.%, and (c) 6 wt.%. The solid loading was 50 wt.% HA (taken from Fu) [117]

Araki et. al. used an aqueous component that was purely camphene. The dendrites formed by the camphene during solidification left a ceramic body with circular interconnected porosity (Figure 25) [119]. Using camphene, Soon et al. were able to fabricate structures

with highly aligned porosity, as opposed to the more random orientation produced by Araki by unidirectionally freezing at the day length scale (1, 2, 3 days) (Figure 26) [120]. They obtained samples with a porosity of 62-65 vol.% and pore sizes that decreased from 166 μm to 122 μm as the freezing time increased from 1 day to 3 days while compressive strength increased from 6.2 ± 1.3 MPa to 9.3 ± 1.6 MPa [120].

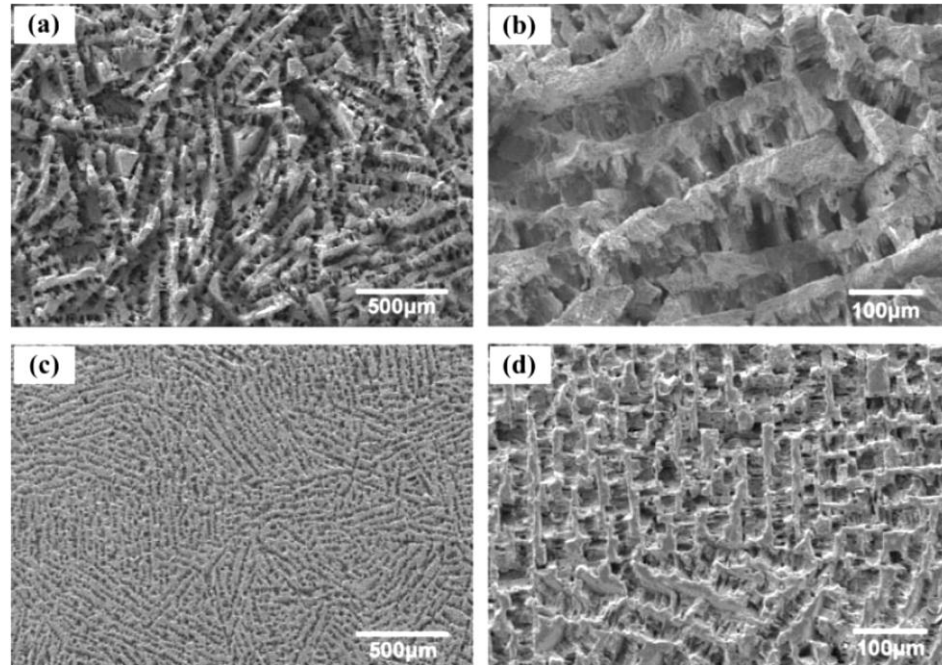


Figure 23. Effects of glycerol concentration on the microstructure of the sintered HA sample (a), (b) 5 wt. %; (c), (d) 20 wt. %. (The cross section is perpendicular to the freezing direction.) (taken from Fu) [118]

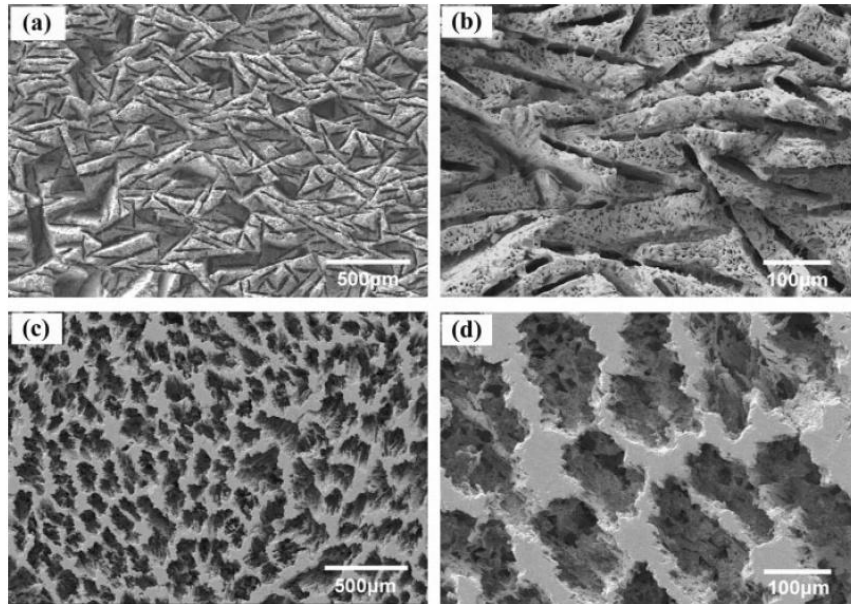


Figure 24. Effects of dioxane concentration on the microstructure of the sintered HA sample (a), (b) 30 wt. %; (c), (d) 60 wt. %. (The cross section is perpendicular to the freezing direction.) (taken from Fu) [118]

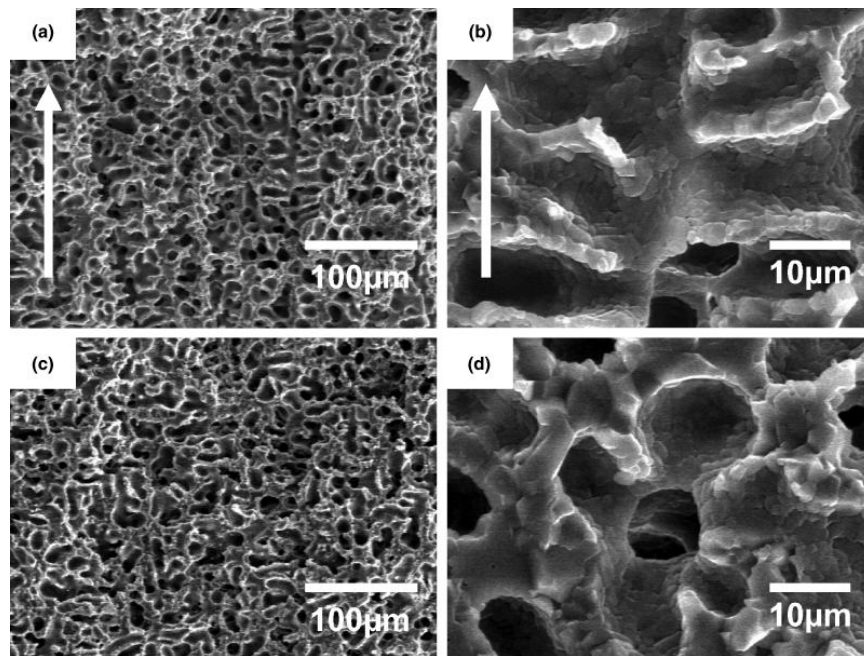


Figure 25. Microstructures of (a), (b) vertical, and (c), (d) horizontal cross-sectional views in the sintered Al_2O_3 , unidirectionally solidified body. Arrows in the figure indicate the solidification direction. (taken from Araki) [119].

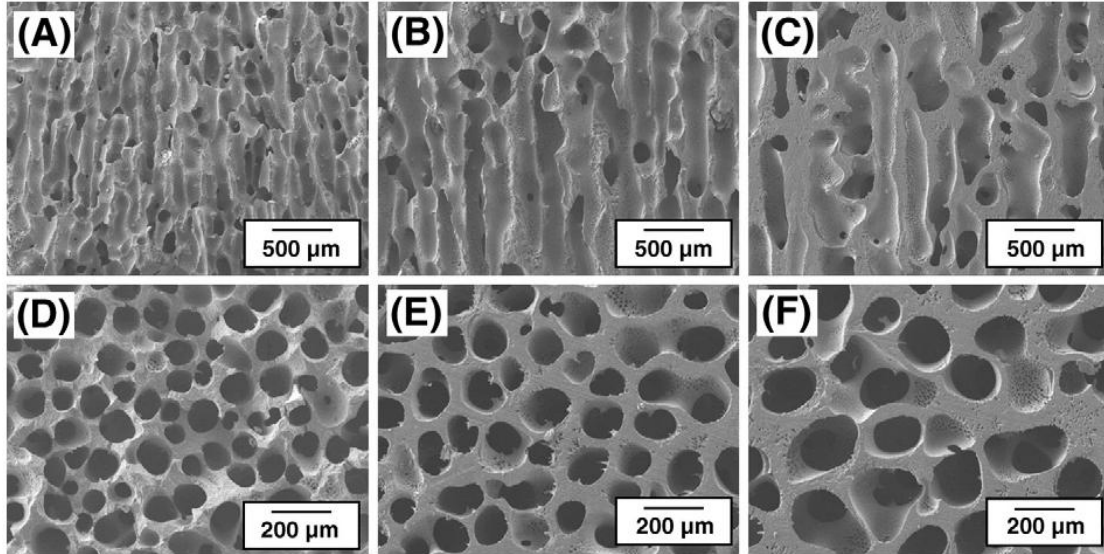


Figure 26. Typical SEM micrographs of the porous calcium phosphate scaffolds produced at various freezing times of 1 day ((A),(D)), 2 days ((B),(E)), and 3 days ((C),(F)), showing highly aligned pore structures. The top ((A),(B),(C)) and bottom ((D),(E),(F)) images represent the pore structures developed parallel and normal to the freezing direction, respectively (taken from Soon) [120].

EXPERIMENTAL METHOD

Natural hydroxyapatite scaffolds

The bovine femur bone (~18 months old) used for this experiment was sourced from a local supermarket. Sample preparation began with removal of the soft tissues including muscle and connective tissue. The muscles and tendons were cut away using knife. The cancellous bone was then sectioned out from the proximal end of the femur and cut into $9 \times 9 \times 30 \text{ mm}^3$ slabs using a band saw. A dental water pick was then used to clean away any remaining bone marrow. The bone was then stored in water until heat treatment. The sintering process was as follows: the samples were heated at a rate of $3^\circ\text{C}/\text{min}$ up to a temperature of 1325°C , held for 3 hours, and cooled back to room temperature at a rate of $3^\circ\text{C}/\text{min}$. After removal from the furnace, the scaffolds were sectioned roughly into $5 \times 5 \times 7 \text{ mm}^3$ rectangular prisms using razor wire. Final sanding was done on 800 grit sandpaper to get the samples down to size as necessary.

Synthetic hydroxyapatite scaffolds by freeze casting

The freeze casted HA scaffolds were developed using a method similar to that outlined by Deville et al. [101]. Ceramic slurries were prepared by mixing water with ammonium polymethacrylate anionic dispersant (Darvan 811), an organic binder (1 wt. %, polyvinyl alcohol (PVA)), polyethylene glycol (PEG 300, Sigma-Aldrich, St. Louis, MO) and HA powder (Hydroxyapatite#30, Trans-Tech, Adamstown, MD). The diameter of the HA powders ranged from 2-5 μm with an average diameter of 2.4 μm . Three

slurries were made using 20 vol.% HA, 30 vol.% HA, and 35 vol.% HA. Table 4 below details the composition of each slurry.

Table 4. Recipes for ceramic slurries with 20 vol.% hydroxyapatite (HA), 30 vol.% HA, and 35 vol.% HA. Values are given in wt.%.

Component	20 vol.% HA	30 vol.% HA	35 vol.% HA
	Wt. %	Wt. %	Wt. %
Darvan 811	0.43%	0.56%	0.61%
PVA	1.07%	1.39%	1.52%
PEG 300	0.43%	0.56%	0.61%
HA	42.92%	55.71%	60.98%
H ₂ O	55.15%	41.78%	36.28%

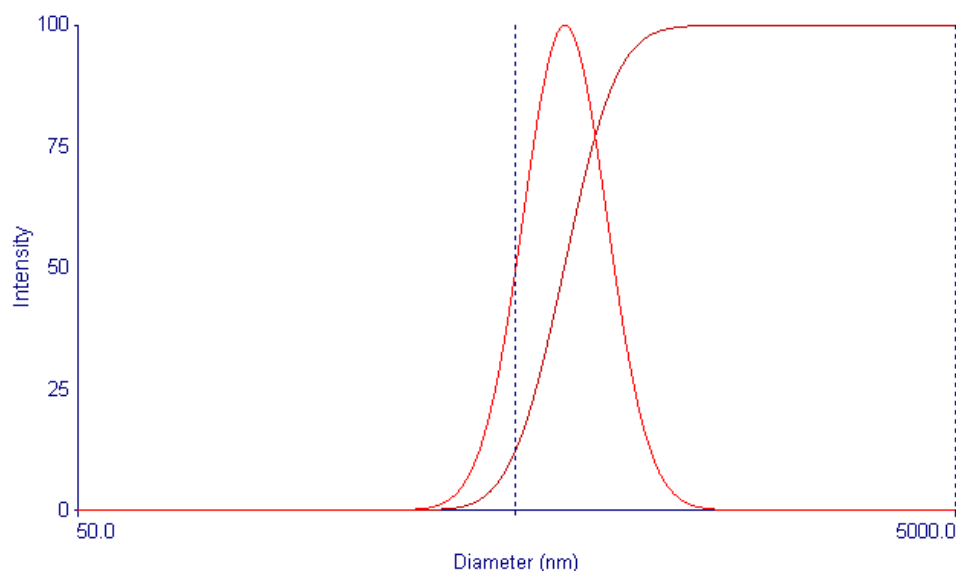


Figure 27. Particle size analysis of the Trans-Tech hydroxyapatite powder. The average particle diameter was 646.4 nm.

The slurry was then ball-milled with ½” diameter alumina media for 24 hours. The slurry was then transferred into a beaker and set into a vacuum chamber filled with ice. The

slurry was degassed with constant stirring under vacuum until free of air. A dimensioned drawing of the PTFE mold, copper lid, and cold finger is shown in Figure 28 and Figure 29 shows a schematic diagram of the freeze-casting apparatus. Petroleum jelly was applied to lower inner rim of a cylindrical polytetrafluoroethylene (PTFE) mold which was then set atop a polished copper lid. The petroleum jelly was used as a seal to prevent leakage from the mold once the slurry was poured in. The mold and lid were set on top of the cold finger and heat was applied until the assembly stabilized at a temperature of 20°C. The ceramic slurry was subsequently poured into the mold. Freezing rates of 1, 5, and 10°C/min were controlled by liquid nitrogen, a ring heater, a thermocouple, and a PID controller. After freezing was complete, the mold was removed from the copper lid and warmed for approximately 1-2 min at 37°C to ease the removal process. After the freeze-cast sample was removed from the mold, it was then transferred to a freeze dryer (Freeze Dryer 8, Labconco, Kansas City, MO) operating at -100°C and 1.3 kPa for a period of 24 hours. Once all water was removed, the green bodies were sintered in an air furnace (1216BL, CM Furnaces Inc., Bloomfield, NJ) at 1350°C for three hours with heating and cooling rates of 2°C/min. After removal from the furnace, the rods were cut into 7 mm thick disks which were then cut down into $5 \times 5 \times 7 \text{ mm}^3$ rectangular prisms with a diamond coated saw blade. The long 7mm edges were oriented parallel with the growth direction of the scaffold.

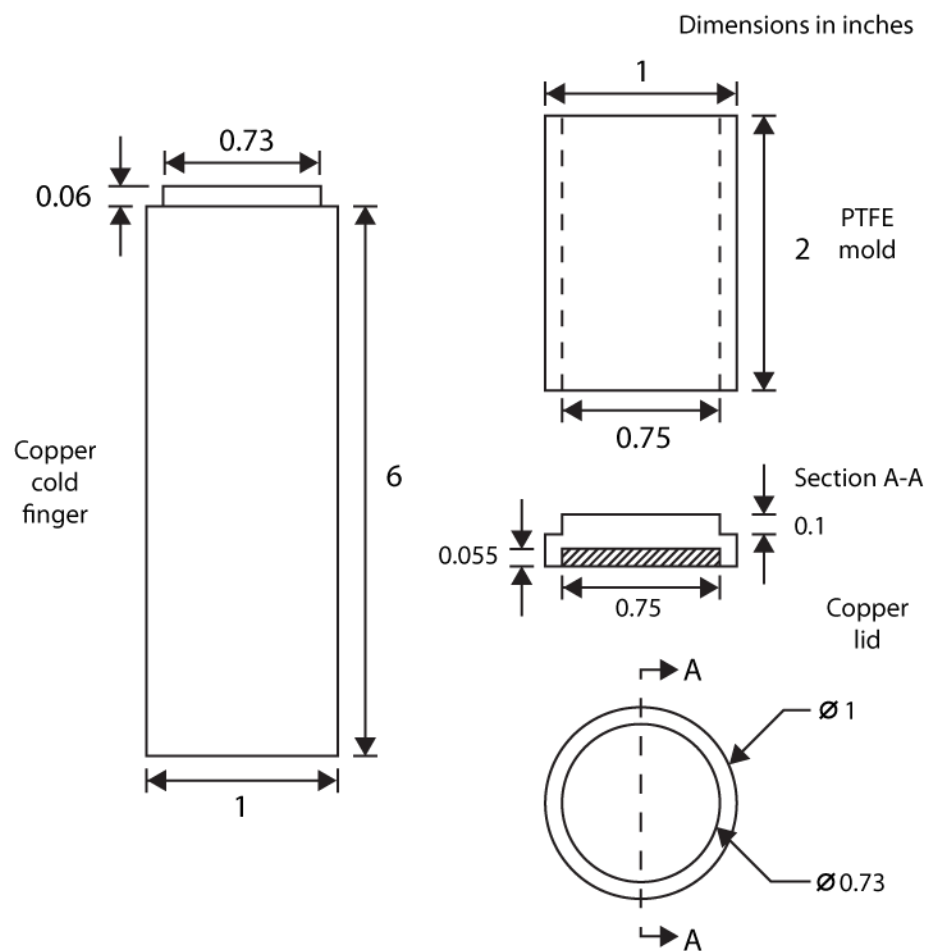


Figure 28. Dimensioned drawing of copper cold finger, PTFE mold, and copper lid.

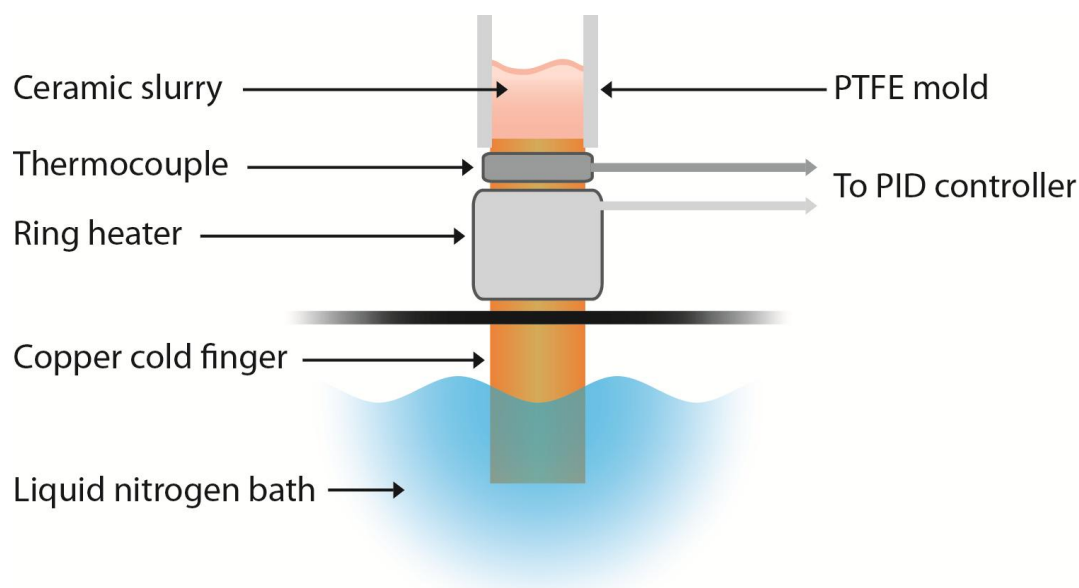


Figure 29. Schematic diagram of the freeze-casting apparatus.

Polymer Infiltration

The natural HA scaffolds were infiltrated with polymethylmethacrylate (PMMA) using an acrylic embedding kit (Electron Microscopy Sciences, Hatfield, PA). Methyl methacrylate monomer and a catalyst were mixed in a 12:1 ratio by weight prior to setting the cancellous scaffold in polymer. The mold containing the scaffold and polymer were placed under vacuum until fully degassed. The mold was then set in an oven at 30°C until polymerization was complete. The synthetic freeze-casted scaffolds were placed in an oven dried vial and 20 mg 2,2'-azobisisobutyronitrile (AIBN) (Aldrich, St. Louis, MO) was added. The vial was then flushed with argon and injected with 2 ml methyl methacrylate (MMA) (Aldrich). After injection, the sample was placed under vacuum and held until bubbling stopped. This step was used to ensure that the MMA infiltrated into the pores of the ceramic scaffold. The vial was then flushed with argon

again, and placed in a 50°C oil bath for 18 hours. No stir-bar was used during the polymerization out of concerns of damaging the ceramic.

Compression Testing

Compression testing of samples was carried out on an Instron machine (Instron 3342, Instron, Norwood, MA) using a 500N load cell for the natural scaffolds and a 30kN load cell for all other samples. Each test was carried out using stainless steel platens at a crosshead velocity of 10^{-3} mm/sec. Prior to testing, a light coating of petroleum jelly was applied to the platens to eliminate potential edge effects. Strength was measured as the ultimate compressive strength correlating to the highest peak in the stress-strain curve. The Young's modulus was measured as the slope of the linear elastic region of the stress-strain curve according to Equation 6:

Equation 1

$$E = \frac{\Delta\sigma}{\Delta\varepsilon} \quad (6)$$

Where E is the Young's modulus, $\Delta\sigma$ is the change in stress, and $\Delta\varepsilon$ is the change in strain.

Physical & Chemical Characterization

Physical characterization was carried out by scanning electron microscopy (SEM), x-ray diffraction (XRD), and particle size analyzer. The SEM samples were set onto an aluminum sample holder and sputter coated with iridium using a EMITech K575X Sputter Coater (EMITech Inc., Fall River, MA). SEM images were taken on a Phillips/FEI XL30 environmental scanning electron microscope (ESEM) (FEI Co., Hillsboro, OR) using an accelerating voltage of 20 kV and a spot size of 3. The XRD

samples were ground into a fine powder using a mortar and pestle and set into a glass slide for analysis using a Rigaku MiniFlex II (Rigaku Americas, The Woodlands, TX). Particle size analysis was carried out on a ZetaPlus (Brookhaven Instruments Corporation, Holtsville, NY).

RESULTS & DISCUSSION

Natural Scaffolds

Figure 30 compares the structure of untreated cancellous bone with that of the heat treated natural scaffold. The natural cancellous microstructure is intact after heat treatment to form the natural scaffolds (Figure 30b). The pore sizes in both the bone and the scaffold range from 100 – 300 μm and are highly interconnected. A treatment similar to one used by Taniguchi et. al. was selected as it has successfully been implanted with good results in human trials [121]. After heat treatment, XRD analysis confirmed that the scaffold was hydroxyapatite (Figure 31).

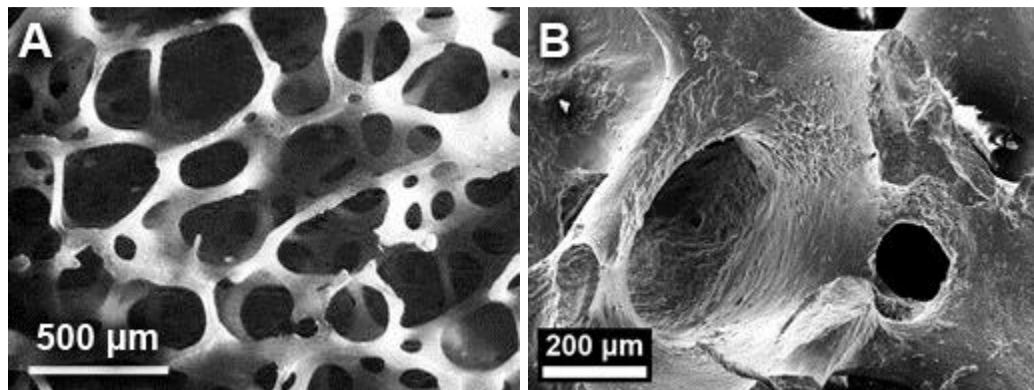


Figure 30. a) Micrograph of untreated bovine cancellous bone. b) SEM image of natural scaffold (heat treated at 1325°C).

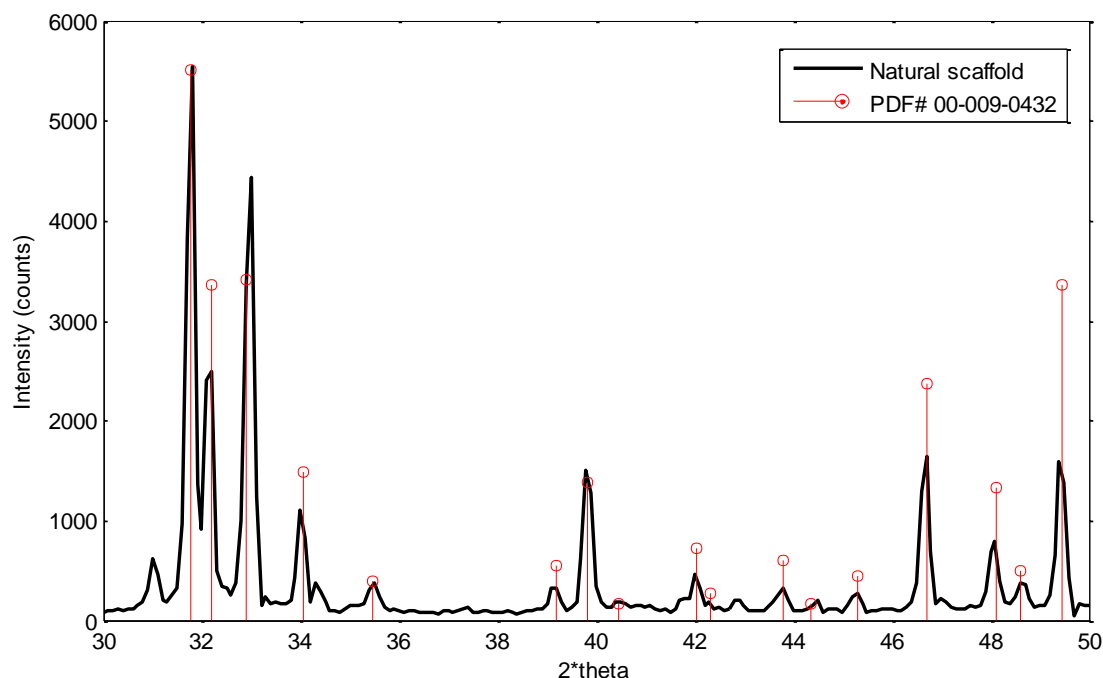


Figure 31. X-ray diffraction pattern of cancellous bone heated at 1325°C for 3 hours (natural scaffold) compared with hydroxyapatite reference peaks (PDF# 00-009-0432).

Table 5 compares the physical and mechanical properties of natural bone and the fabricated scaffolds. The natural scaffolds had higher strength and modulus compared to cancellous bone. Comparison of the stress-strain behavior of cancellous bone (Figure 32) and the natural scaffold (Figure 33) reveal two very different behaviors under compressive loading. Figure 32 gives representative stress vs. strain curves of cancellous bone at three different relative densities where the relative density is the density of the cancellous bone (ρ) divided by density of solid HA (ρ_s) [85]. Cancellous bone, like a cellular solid, has a region of constant stress after yielding that finally leads to another increase in stress on densification. The natural scaffold (Figure 33), on the other hand, behaved in a brittle manner due to the continuous mineral phase formed after heat treatment.

Table 5. Physical and mechanical properties of hydrated cortical bone [83], cancellous bone [82], and natural scaffold (heated bovine cancellous bone). (ρ = bulk density, σ = compressive strength, E = Young's modulus).

	Vol. % mineral	Porosity (%)	Pore size (μm)	ρ (g/cm^3)	σ (MPa)	E (GPa)
Cortical bone	30-40	5 – 10	10 – 50	2.0	110 – 150	18 – 22
Cancellous bone	30-40	75 – 85	300 – 600	0.2 – 0.5	2 – 6	0.1 – 0.3
Natural HA scaffolds	100	50–90	100–600	0.3–1.3	0.4–9.7	0.1–1.2

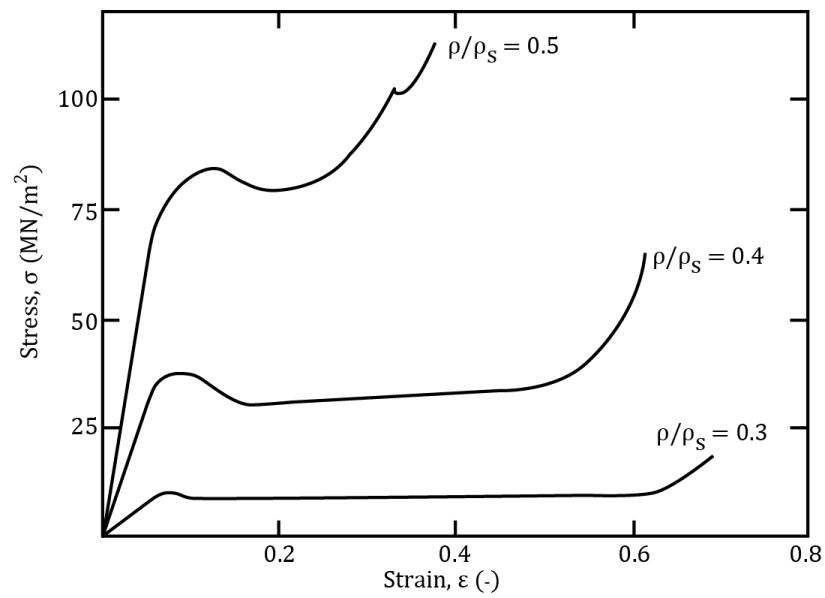


Figure 32. Stress-strain curves for cancellous bone. As relative density increases, Young's modulus and compressive strength increase. The strain at which the cell walls touch and densification occurs decreases (taken from Gibson) [85].

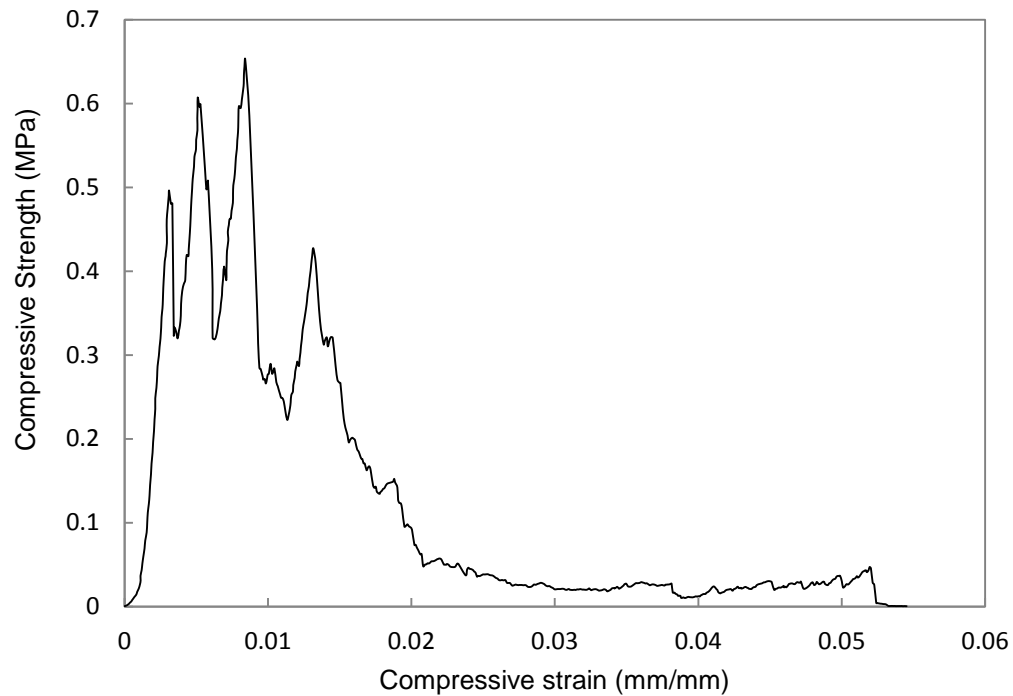


Figure 33. Representative behavior of natural scaffold under compressive loading ($\dot{\epsilon} = 0.001$ mm/sec).

Natural scaffolds have some advantages as a bone implant solution. They are highly biocompatible since they are composed of the same HA minerals found within natural bone. They also have high porosity that is well interconnected and conducive to cell and vascular ingrowth. This type of scaffold has been documented to work well *in vitro* and *in vivo* [122-124] and is also available commercially in one form as Bio-Oss®. These features, however, belie the deficits in the cancellous structure of the scaffolds in load-bearing roles. High porosity also means low density and low strength, the latter property being critical for a load-bearing implant. Natural scaffolds may serve adequately in areas of the skeletal system that experience little to no loads; outside of these low stress regions, a different type of scaffold may be more advantageous.

Natural scaffold composite

Table 7 compares the physical and compressive mechanical properties of the natural HA scaffolds, PMMA, and the natural HA-PMMA composites. The natural HA-PMMA composite exhibited a strength and Young's modulus of 55 MPa and 4.5 GPa, respectively - much stronger than natural cancellous bone. Comparison of the stress/strain behavior of the composite (Figure 34) and natural cancellous bone (Figure 32) reveal curves that are remarkably similar. By filling the voids with PMMA, mechanical properties were increased while porosity, a trait desirable in bone substitutes, was lost. The strength of the natural HA-PMMA composite is noticeably lower than that of pure PMMA, likely due to a lack of interfacial bonding. Figure 35 shows visibly smooth channels that have been vacated by the sintered cancellous bone.

Table 6. Physical and compressive mechanical properties of natural HA scaffolds, pure PMMA, and natural HA-PMMA composites. (ρ = bulk density, σ = compressive strength, E = Young's modulus).

	ρ (g/cm ³)	σ (MPa)	E (GPa)
Natural HA scaffold	0.8	4.5	0.6
PMMA	1.2	80	2
Natural HA scaffold + PMMA	1.5	55	4.5

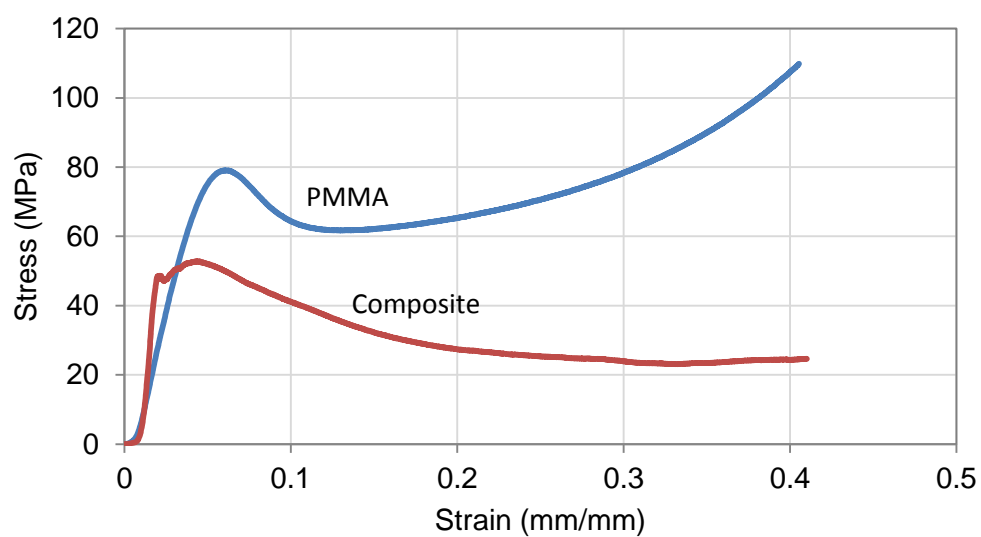


Figure 34. Representative curves of the compressive behavior of pure PMMA compared against natural scaffold composite. The PMMA exhibited higher strength (80MPa) while the natural scaffold composite had a higher Young's modulus (55 MPa).

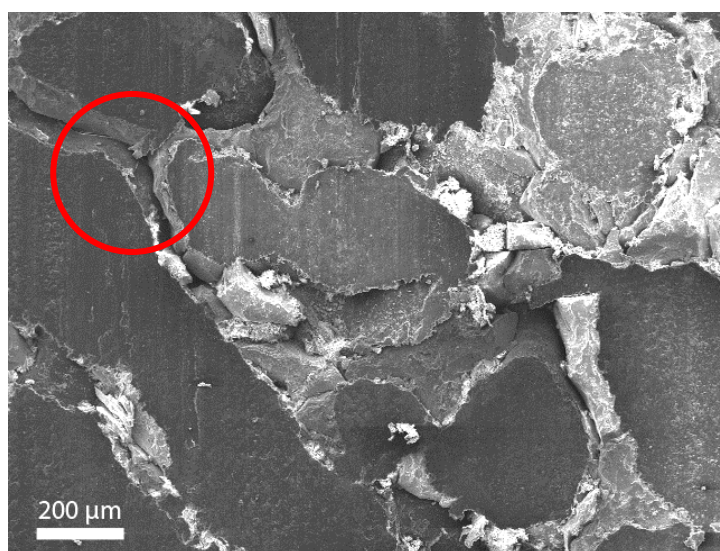


Figure 35. SEM image PMMA infiltrated natural hydroxyapatite scaffold. Circled in red is a smooth channel formerly occupied by part of the natural scaffold.

Synthetic scaffold

After heat treatment, XRD analysis confirmed that the sintered scaffolds were hydroxyapatite (Figure 36). In contrast to the natural scaffolds, the synthetic scaffolds show a well aligned lamellar structure (Figure 37-Figure 39). Visual inspection of the SEM images in Figure 37-Figure 39 shows that lamellae spacing reduced as cooling rates were increased, whereas the thickness of the lamellae decreased as the solid loading was increased. These are useful features that may allow the construction of lamellar scaffolds with microstructures very similar to lamellar bone, a precursor to the formation of Haversian systems. Also evident in the figures are interlamellar bridges that may contribute to improving the fracture toughness of the scaffold by mitigating crack propagation. Representative stress vs. strain curves in Figure 40 show that at a given slurry concentration (30 vol.% in this case), both strength and Young's modulus increase with increasing cooling rates. The scaffolds with higher solid loadings exhibited higher strengths and Young's moduli, reaching a maximum strength and Young's modulus of 95.1 MPa and 14.9 GPa, respectively, at a concentration of 35 vol. % HA and cooling rate of 10°C/min.

Table 7. Comparison of the mechanical and physical properties of cortical bone and the synthetic HA scaffolds. (ρ = bulk density, σ = compressive strength, E = Young's modulus).

	Vol. % mineral	Porosity (%)	Pore size (μm)	ρ (g/cm^3)	σ (MPa)	E (GPa)
Cortical bone	30-40	5 – 10	10 – 50	2.0	110 – 150	18 – 22
Synthetic HA scaffolds	100	50–70	10–50	0.9–1.7	0.7–95.1	0.1–14.9

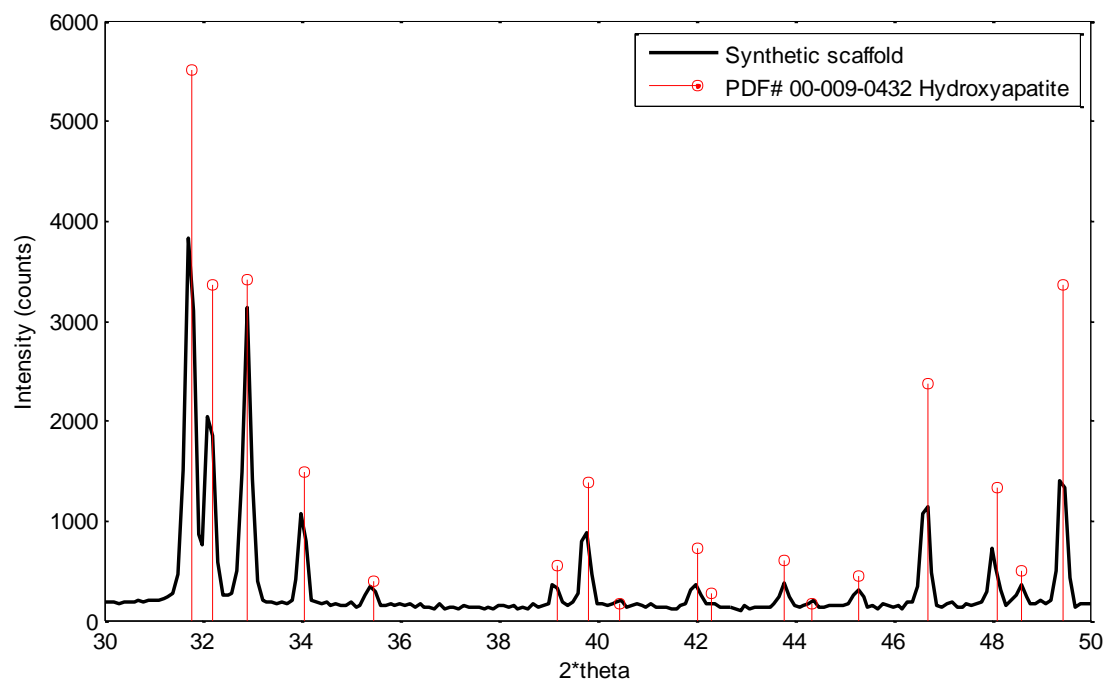


Figure 36. X-ray diffraction pattern of synthetic scaffold treated at 1350°C for 3 hours compared with hydroxyapatite reference peaks (PDF# 00-009-0432).

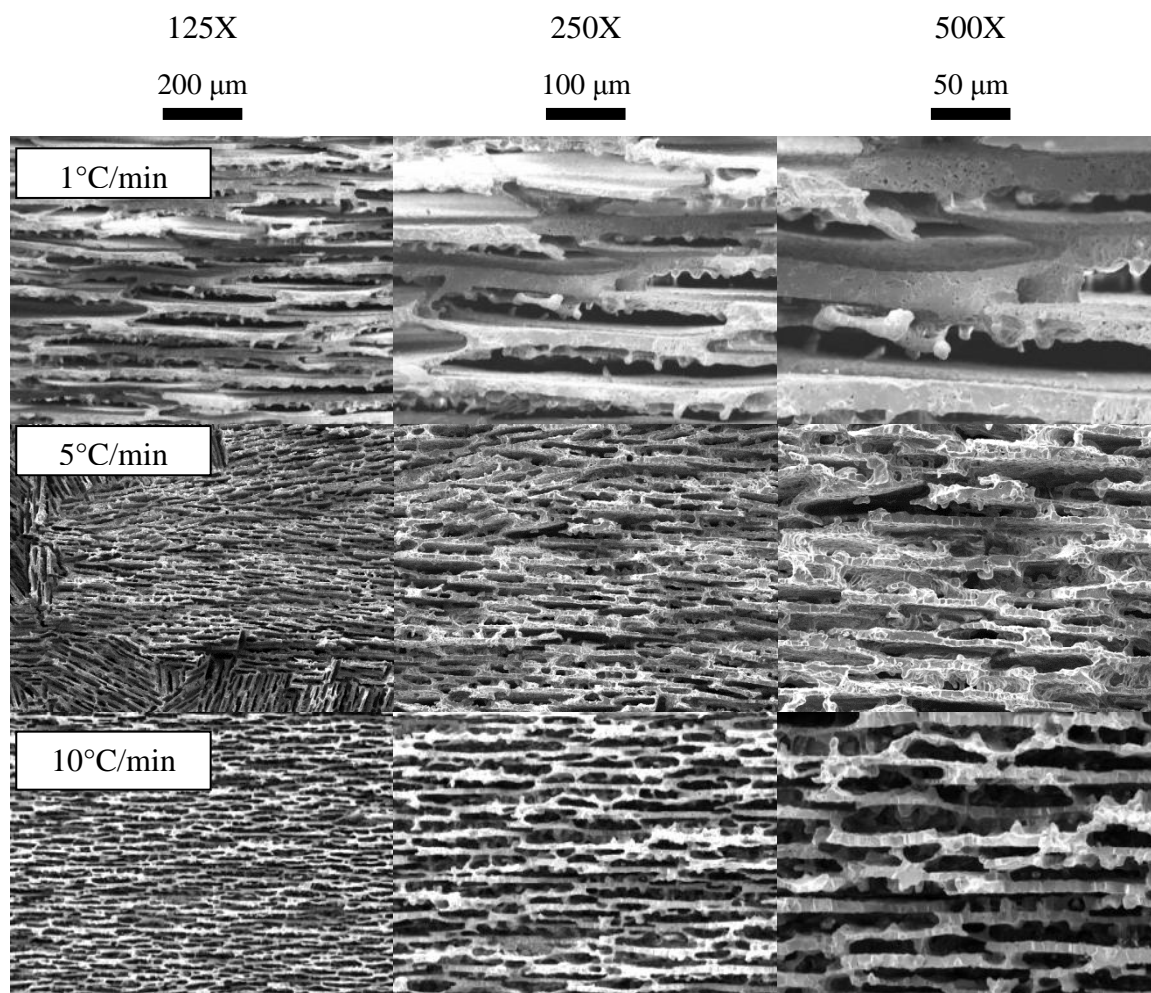


Figure 37. SEM images of synthetic scaffold fabricated from 20 vol. % HA and cooled at various rates. The cooling rate for each row is denoted by the inset box.

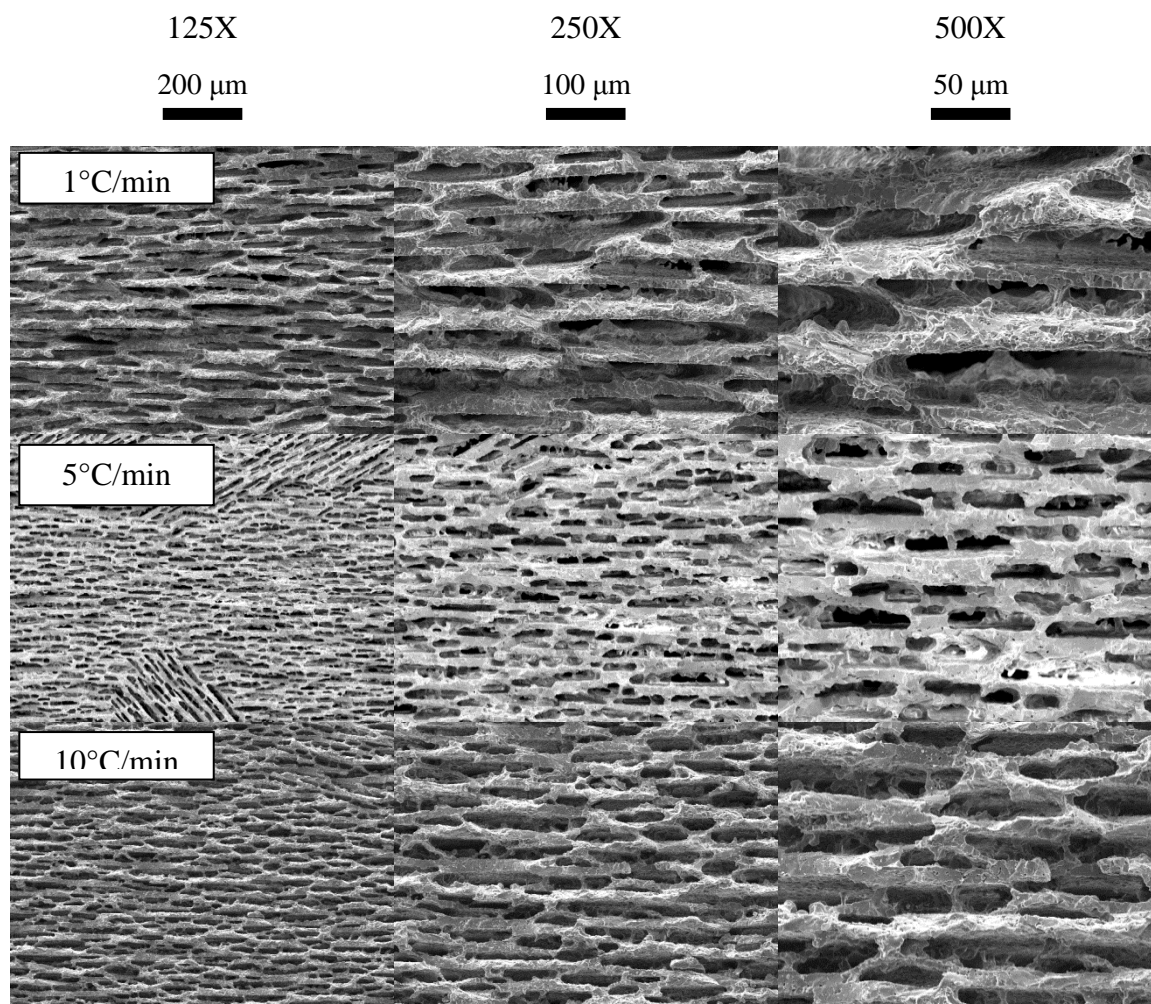


Figure 38. SEM images of synthetic scaffold fabricated from 30 vol.% HA and cooled at various rates. The cooling rate for each row is denoted by the inset box.

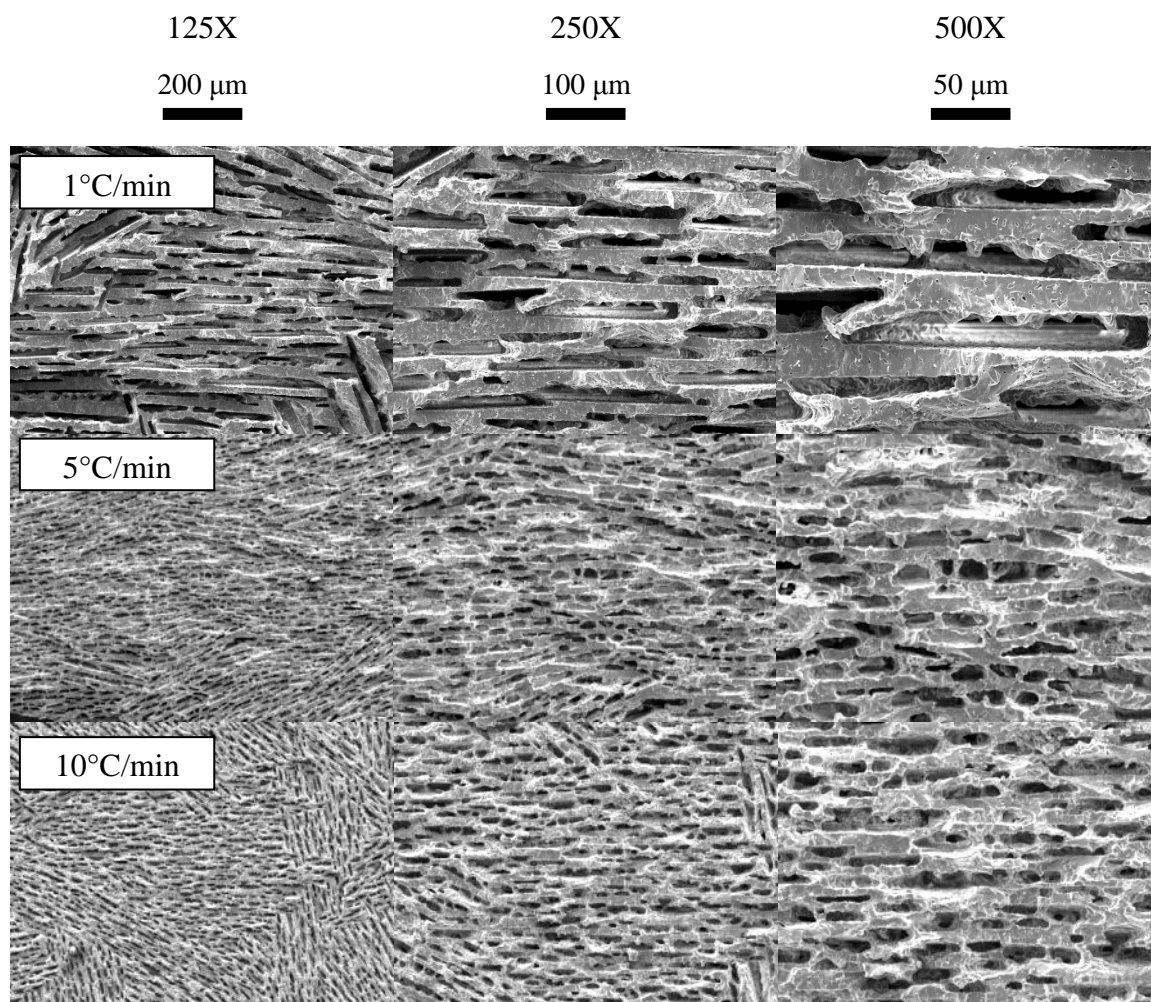


Figure 39. SEM images of synthetic scaffold fabricated from 35 vol.% HA and cooled at various rates. The cooling rate for each row is denoted by the inset box.

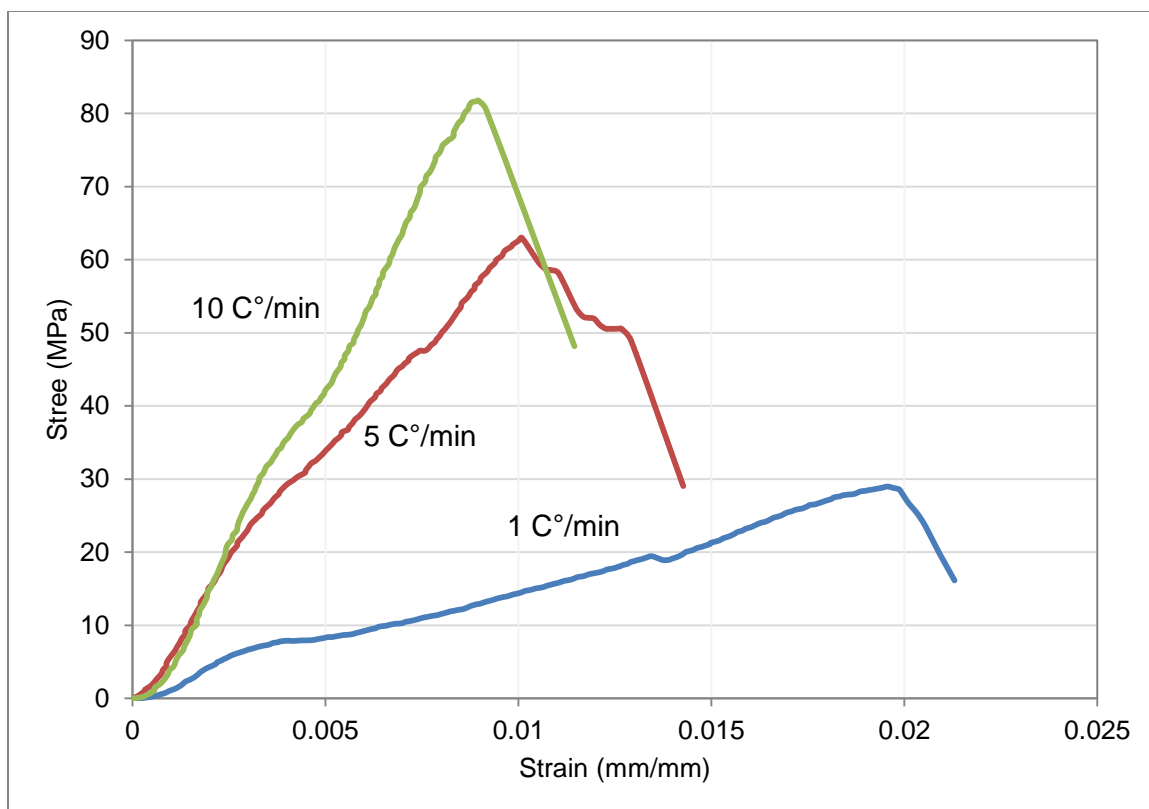


Figure 40. Representative stress vs. strain plot of the synthetic scaffolds (30 vol.% cooled at rates of 1, 5, and 10 °C/min).

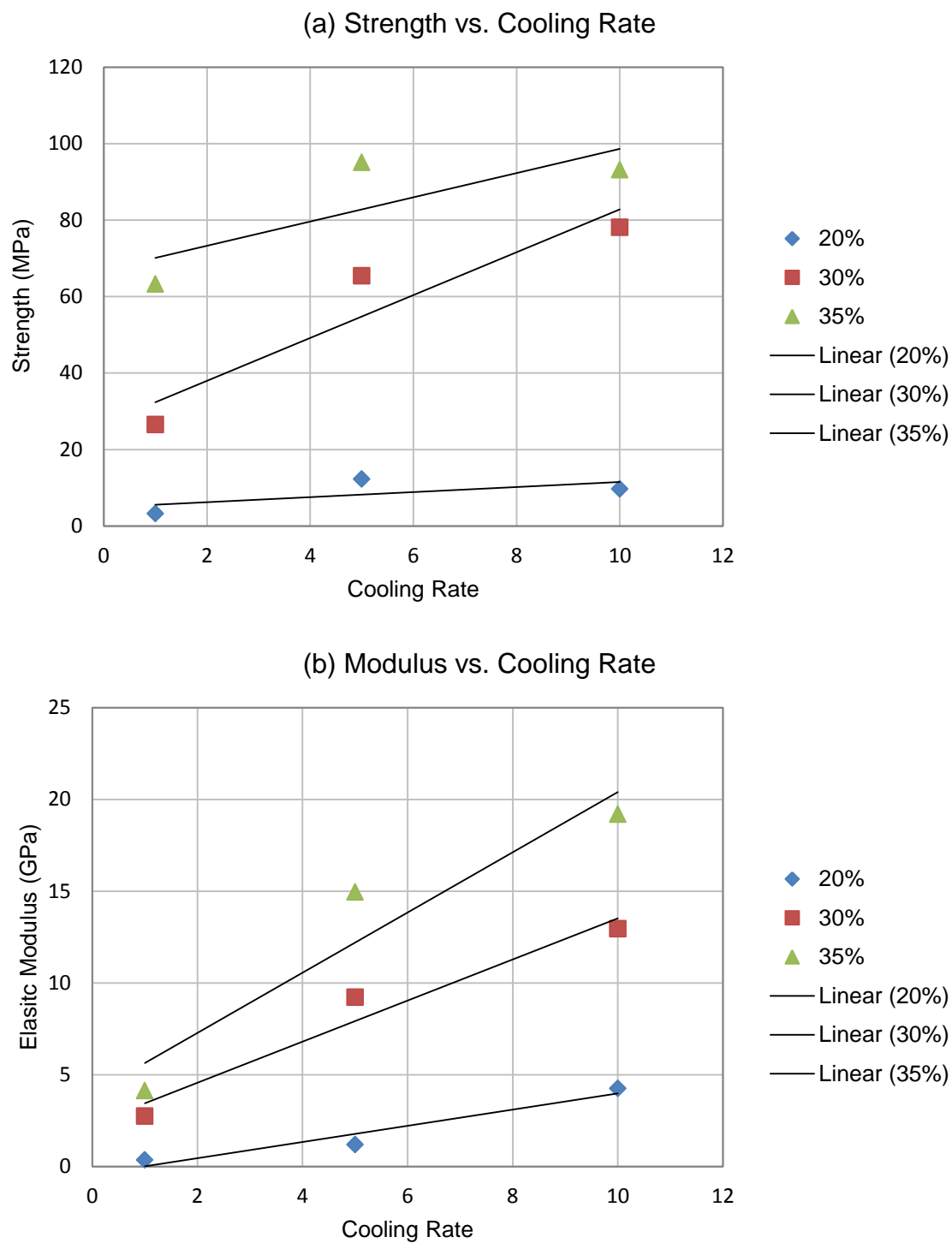


Figure 41. (a) The strength of the synthetic scaffold increases logarithmically as a function of the cooling rate. (b)

Synthetic scaffold composite

Based on preliminary results, the synthetic HA-PMMA composites, with an initial slurry concentration of 20 vol.% HA frozen at 1°C/min, exhibited a strength of 42 MPa and an Young's modulus of 0.8 GPa; this was an order of magnitude increase in strength and a two-fold increase in modulus over the initial scaffold ($\sigma = 3.2$, $E = 0.4$ GPa). While these gains are promising, in Figure 42(a) voids are visible where PMMA has not fully penetrated the scaffolds. In Figure 42(b), significant delamination of the synthetic HA-PMMA composite is visible. Between the buckled layers of PMMA are remnants of the inorganic HA phase that has crumbled away due to brittle failure. This indicates a lack of interfacial bonding between the HA and PMMA layers.

To supplement mechanical bonding with a chemical bond, HA surface modifications such as coupling agents and polymer grafting are being explored to design a composite with improved mechanical properties. Deb et. al. found success using both techniques for HA-polyethylene composites that either used a silane coupling agent or the coupling agent in addition to grafted polyethylene [125].

A chemically bonded biphasic composite would serve well as a bone substitute. It would combine the strength of a lamellar mineral phase with a tough polymer to create a composite that in many respects mimics the mechanical and physical properties of natural cortical bone. This freeze-cast composite has the potential to replace autogenic and allogeneic bone substitutes; substantially lowering health care costs due to its simple and non-toxic fabrication methods.

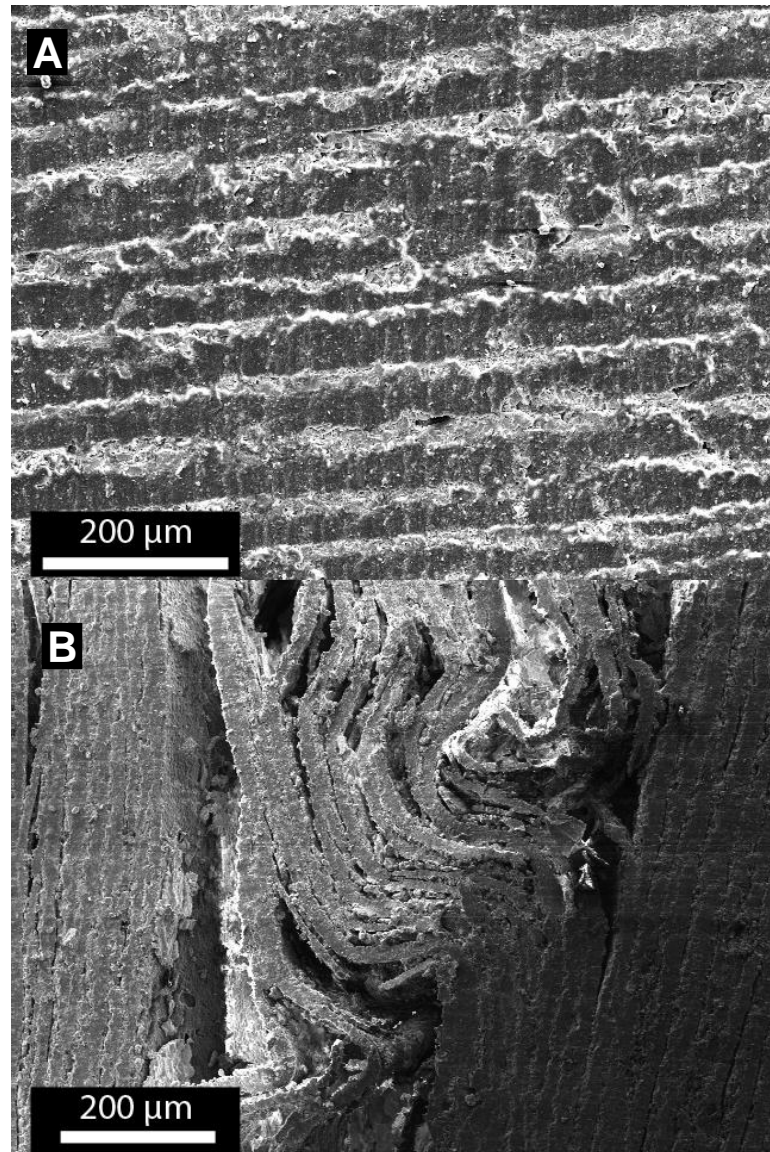


Figure 42. (a) Synthetic freeze-casted hydroxyapatite (HA) scaffold infiltrated with PMMA. (b) Fracture surface of the synthetic HA-PMMA composite after compressive failure. The light bands are the inorganic HA phase and the dark bands are the organic PMMA.

Summary of Infiltrated Scaffolds

Figure 43-Figure 44 summarize the mechanical testing results of the natural scaffold and synthetic scaffold. The test data was overlaid with a fit line using relationships given by Gibson (Eq. 6, 7) between relative strength or relative Young's modulus and the relative density where σ^* , E^* , and ρ^* are properties of the tested scaffolds and σ_s , E_s , and ρ_s are the properties of cortical bone ($\sigma_s = 272$ MPa, $E_s = 20$ GPa, $\rho_s = 2$ gm/cm³) [85]. The constants C_1 , C_2 , n , and m are fitting parameters where C_1 and C_2 are XXX and n and m define the slope in the log-log plots.

$$\frac{\sigma^*}{\sigma_s} = C_1 \left(\frac{\rho^*}{\rho_s} \right)^m \quad (6)$$

$$\frac{E^*}{E_s} = C_2 \left(\frac{\rho^*}{\rho_s} \right)^m \quad (7)$$

For the plots in Figure 43-Figure 44, C_1 and C_2 were set equal to 1 and n and m were set equal to 10 and 3, respectively. A value of $n = 10$ reveals that the strength of the synthetic scaffolds is highly sensitive to changes in density and less so for the Young's modulus. The natural scaffold composite data points, however, stack in a near vertical line. This is most likely due to the infiltrated PMMA becoming the dominant continuous phase within the composite, leading to more consistent test results within a small range of densities. The bone samples used to make these scaffolds were cut out in close proximity to each other, another factor that may explain the results. As tested, the natural composites are not an optimal scaffold. Within the body, bone varies in mechanical and

physical properties throughout the body, requiring a scaffold whose properties can be easily controlled. In this respect the synthetic scaffold possesses an advantage with its easily tunable properties.

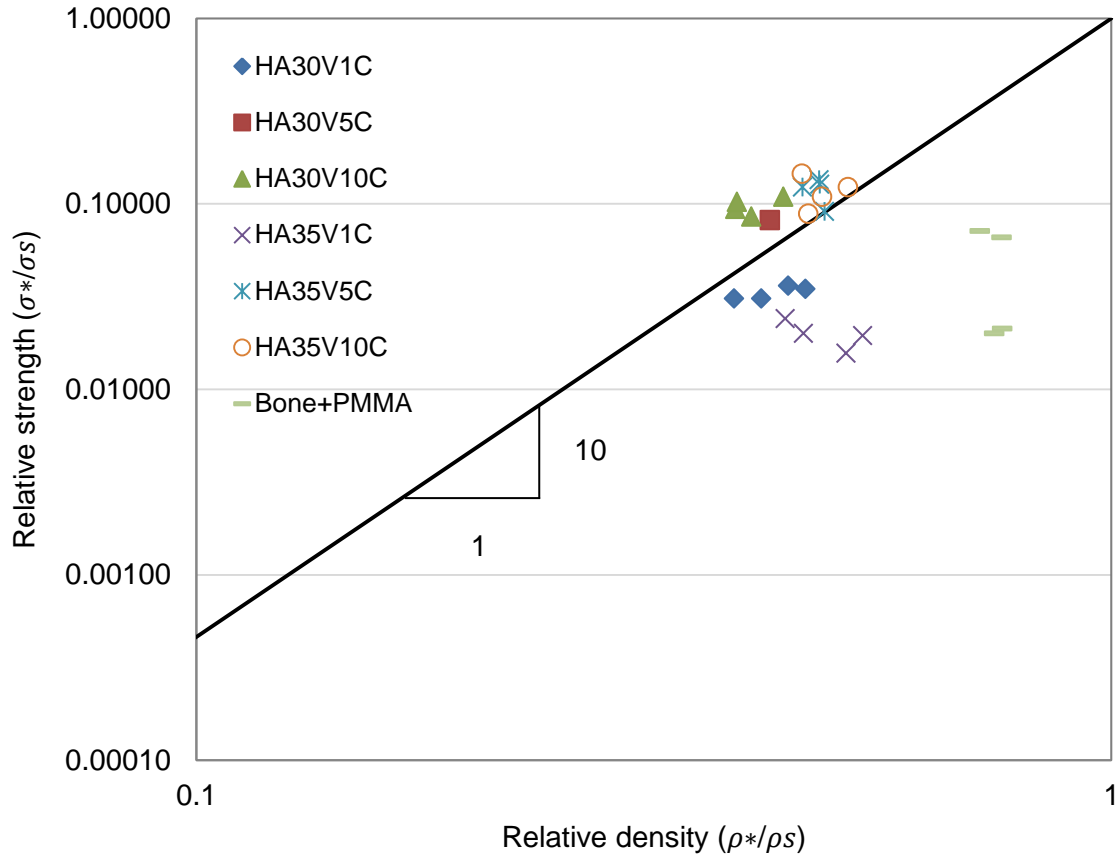


Figure 43. Log-log Plot of the relative strength versus the relative density of the synthetic scaffolds and natural scaffold composite.

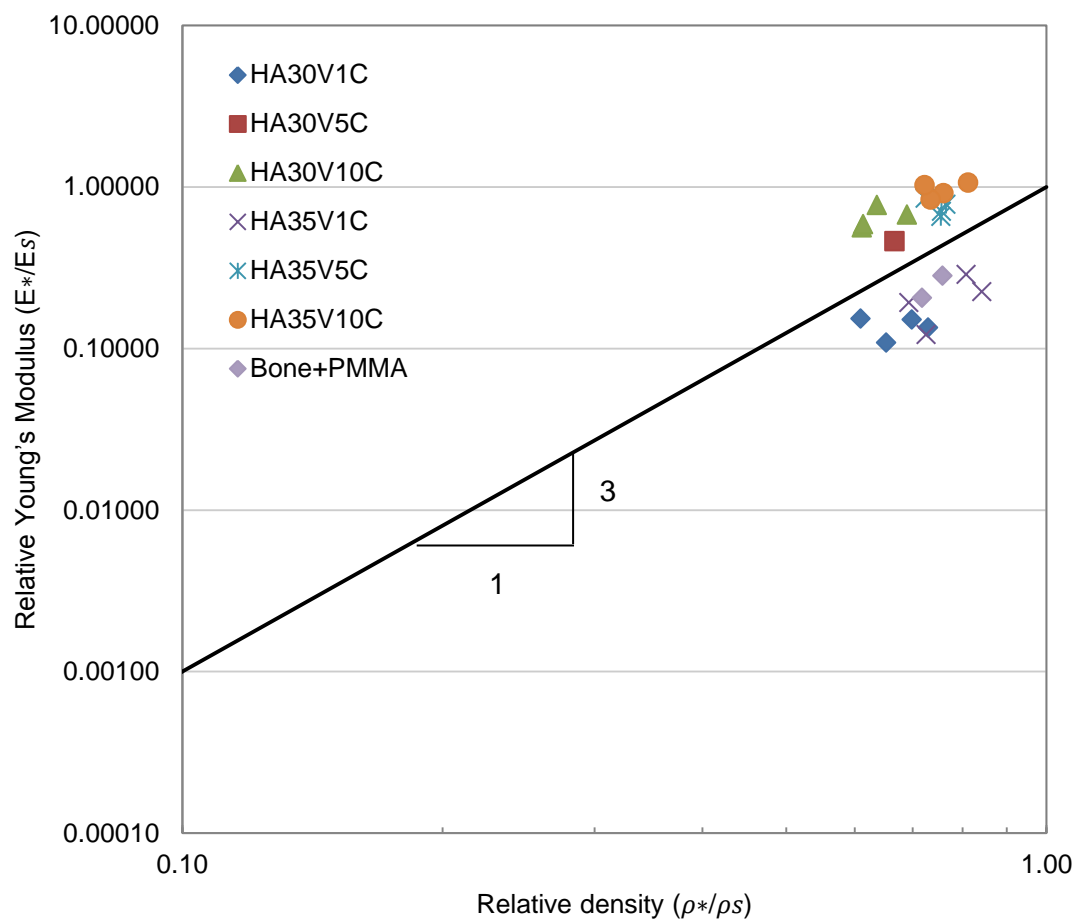


Figure 44. Plot of the relative Young's modulus versus relative density of the synthetic scaffolds and natural scaffold composite.

CONCLUSION

The natural scaffold has shown to be at least as strong and as stiff as cancellous bone. Prior work by Minamide et. al. has even proven its efficacy as a bone substitute material with the addition of certain growth factors [123-124]. Infiltrating the natural scaffolds with PMMA led to a further increase in strength and stiffness that, while higher than cancellous bone, was still far below that of cortical bone. However, improvements in mechanical properties came at the expense of porosity. In this area, the synthetic scaffolds show the most promise.

The freeze casting procedure produced scaffolds with a well ordered lamellar microstructure. They possess strength and stiffness approaching that of cortical bone, a good sign for a potential load-bearing bone substitute. Preliminary data showed that infiltrating the synthetic scaffolds with a polymer phase increases all mechanical properties. Infiltration was successful, but requires further work to optimize the process by introducing a surface modification to chemically bond the two phases. Compression testing clearly showed that there was no interfacial bonding, as evidenced by the buckling of the polymer and ejection of the mineral phase. Improvements in this area are necessary to design a high performance bone substitute with controllable mechanical and physical properties that can compete with autogenic and allogeneic cortical bone tissue.

Recommendations for Future Work

Future work with synthetic scaffolds needs to address two major areas. First, the scaffold morphology requires further exploration. Current freeze casting techniques primarily utilize water as the sacrificial phase. While it produces a nicely aligned lamellar microstructure, the scaffolds lack interconnected porosity. The second area is in polymer infiltration. The polymer and mineral phases must bond chemically to optimize mechanical properties and open the door for different morphologies. Rather than completely filling pores, the polymer phase could be used as a film which would add strength without sacrificing porosity. A polymer film has the added advantage of being able to carry and release drugs or growth factors over a large surface area.

Once the previous concerns are addressed, polymer infiltrated synthetic scaffolds will have the most promise as a bone graft substitute material. They would possess the right balance of mechanical, physical, and chemical properties to replace autogenic and allogeneic bone as a bone graft material. The scaffolds would be low-cost, easy to sterilize, and environmentally friendly. Supply would not be limited like autogenic bone, and there would be no fear of disease transmission like allogeneic bone. Synthetic scaffolds represent the future of bone substitutes!

REFERENCES

1. S.M. Perrin, "Evolution of the internal fixation of long bone fractures. The scientific basis of biological internal fixation: choosing a new balance between stability and biology," *Journal of Bone and Joint Surgery* 84(8), 1093-1100 (2002).
2. C. Laurencin, Y. Khan, S.F. El-Amin, "Bone graft substitutes, Expert Review of Medical Devices 3, 49-57 (2006).
3. M. Cabraja, M. Klein, T.-N. Lehmann, "Long-term results following titanium cranioplasty of large skull defects," *Neurosurgical Focus* 26(6), E10 (2009).
4. G. Kuman, N. Peterson, B. Narayan, "Bicondylar tibial fractures: Internal or external fixation?" *Indian Journal of Orthopaedics* 45(2), 116-124 (2011).
5. J.A. Elo, A.S. Herford, P.J. Boyne, "Implant success in distracted bone versus autogenous bone-grafted sites," *Journal of Oral Implantology* 35(4), 181-184 (2009).
6. C.G. Finkemeier, "Bone-grafting and bone-graft substitutes," *The Journal of Bone and Joint Surgery. American Volume* 84A(3), 454-464 (2002).
7. FR Rose, ROC Oreffo, "Bone Tissue Engineering: Hope vs Hype," *Biochemical and Biophysical Research Communications* 292, 1-7 (2002).
8. S.N. Khan, E. Tomin, J.M. Lane, "Clinical applications of bone graft substitutes," *Orthopedic Clinics of North America* 31(3), 389 (2000).
9. V. Alt, A. Nawab, D. Seligson, "Bone grafting from the proximal tibia," *Journal of Trauma-Injury Infection & Critical Care* 47(3), 555-557 (1999).
10. C. Uerpaiojkit, S. Leechavengvongs, K. Witoonchart, "Primary vascularized distal radius bone graft for nonunion of the scaphoid," *The Journal of Hand Surgery (European Volume)* 25(3), 266-270 (2000).
11. <http://www.sciencequiz.net/jcscience/jcbiology/gapfilling/images/skeleton.gif>
12. W.F. Enneking, H. burchardt, J.J. Puhl, G. Piotrowski, "Physical and biological aspects of repair in dog cortical-bone transplants," *The Journal of Bone & Joint Surgery* 57(2), 237-252 (1975).
13. J.A. Goulet, L.E. Senunas, G.L. DeSilva, M. Lou, "Autogenous iliac crest bone graft: Complications and functional assessment," *Clinical Orthopaedics & Related Research* 339, 76-81 (1997).
14. E.M. Younger, M.W. Chapman, "Morbidity at bone graft donor sites," *Journal of Orthopaedic Trauma* 3(3), 192-195 (1989).

15. R. Kirmeier, M. Payer, M. Lorenzoni, W.A. Wegscheider, F.J. Seibert, N. Jakse, "Harvesting of cancellous bone from the proximal tibia under local anesthesia: Donor site morbidity and patient experience," *Journal of Oral and Maxillofacial Surgery* 65(11), 2235-2241 (2007).
16. J.G. Boorman, J.A. Brown, P.J. Sykes, "Morbidity in the forearm flap donor arm," *British Journal of Plastic Surgery* 40(2), 207-212 (1987).
17. J.J. Tideman, K.L. Garvin, T.A. Kile, J.F. Connolly, "The role of a composite, demineralized bone matrix and bone marrow in the treatment of osseous defects," *Orthopedics* 18(12), 1153-1158 (1995).
18. S. Brown, I. Clarke, P. Williams, "Grafton® demineralized bone matrix combined with cancellous allograft as an autogenous graft substitute in the treatment of fractures and nonunions," *Bioceramics* 218-2, 421-422 (2002).
19. M.A. Shermak, L. Wong, N. Inoue, T. Nicol, "Reconstruction of complex cranial wounds with demineralized bone matrix and bilayer artificial skin," *Journal of Craniofacial Surgery* 11(3), 224-231 (2000).
20. W.R. Sassard, D.K. Eidman, P.M. Gray, J.E. Block, R. Russo, J.L. Russell, E.M. Taboada, "Augmenting bone with Grafton demineralized bone matrix for postlateral lumbar spine fusion: Avoiding second site autologous bone harvest," *Orthopedics* 23(10), 1059-1064 (2000).
21. H.J. Hass, H. Krause, S. Kroker, W. Wagemann, F. Meyer, "Bone formation using human demineralized bone matrix (Grafton ®) for the treatment of bone cysts in children," *European Journal of Pediatric Surgery* 17(1), 45-49 (2007).
22. B. Peterson, P.G. Whang, R. Iglesias, J.C. Wang, J.R. Lieberman, "Osteoinductivity of commercially available demineralized bone matrix – Preparations in a spine fusion model," *Journal of Bone and Joint Surgery – American Volume* 86A(10), 2243-2250 (2004).
23. J.Z. Gao, D. Knaack, V.M. Goldberg, A.L. Caplan, "Osteochondral defect repair by demineralized cortical bone matrix," *Clinical Orthopaedics and Related Research* 427(S), S62-S66 (2004).
24. C.J. Damien, J.R. Parsons, "Bone graft and bone graft substitutes: A review of current technology and applications," *Journal of Applied Biomaterials* 2(3), 187-208 (1991).
25. CDC, "Update: Allograft-Associated bacterial Infections --- United States, 2002," *MMWR* 51(10), 207-210 (2002).
<http://www.cdc.gov/mmwr/preview/mmwrhtml/mm5110a2.htm>

26. M.J. Olszta, X. Cheng, S.S. Je, R. Kumar, Y.-Y. Kim, M.J. Kaufman, E. P. Douglas, L.B. Gower, "Bone structure and formation: A new perspective," *Materials Science and Engineering R* 58, 77-116 (2007).
27. S. Sartori, M. Silvestri, F. Forni, A.I. Cornaglia, P. Tsei, V. Cattano, "Ten-year follow-up in maxillary sinus augmentation using anorganic bovine bone (Bio-Oss). A case report with histomorphometric evaluation," *Clinical Oral Implants Research* 14(3), 369-372 (2003).
28. R.A. Yukna, C.N. Yukna, "A 5-year follow-up of 16 patients treated with coralline calcium carbonate (Biocoral™) bone replacement grafts in infrabony defects," *Journal of Clinical Periodontology* 25(12), 1036-1040 (1998).
29. S.K. Nandi, B. Kundu, S.K. Ghosh, D.K. De, D. Basu, "Efficacy of nano-hydroxyapatite prepared by an aqueous solution combustion technique in healing bone defects of goat," *Journal of Veterinary Science* 9(2), 183-191 (2008).
30. B. Klinge, P. Alberius, S. Isaksson, J. Jonsson, "Osseous response to implanted natural bone mineral and synthetic hydroxylapatite ceramic in the repair of experimental skull bone defects," *Journal of Oral and Maxillofacial Surgery* 50(3), 241-249 (1992).
31. K.D. Johnson, K.E. Frirson, T.S. Keller, C. Cook, R. Scheinberg, J. Zerwekh, L. Meyers, M.F. Sciadini, "Long bone defects: A biomechanical, histological, and radiographic analysis," *Journal of Orthopaedic Research* 14(3), 351-369 (1996).
32. H. Oonishi, "Orthopaedic applications of hydroxyapatite," *Biomaterials* 12(2), 171-178 (1991).
33. K. Ohura, M. Böhner, P. Hardouin, J. Lemaitre, G. Pasquier, B. Flautre, "Resorption of, and bone formation from, new β -tricalcium phosphate-monocalcium phosphate cements: An *in vivo* study," *Journal of Biomedical Materials Research* 30(2), 193-200 (1996).
34. W.R. Moore, S.E. Graves, G.I. Bain, "Synthetic bone graft substitutes," *ANZ Journal of Surgery* 71(6), 354-361 (2003).
35. V. V. Meretoja, T. Tirri, V. Ääritalo, X. F. Walboomers, J.A. Jansen, T.O. Närhi, "Titania and Titania-Silica Coatings for Titanium: Comparison of Ectopic Bone Formation within Cell-Seeded Scaffolds," *Tissue Engineering* 13(3), 855-863 (2007).
36. A. Scarano, F. Di Carlo, M. Quaranta, A. Piattelli, "Bone Response to Zirconia Ceramic Implants: An Experimental Study in Rabbits," *Oral Implantology* 29(1), 8-12 (2003).
37. G. Khang, J.M. Rhee, P. Shin, I.Y. Kim, B. Lee, S.J. Lee, Y.M. Lee, H.B. Lee, I. Lee, "Preparation and Characterization of Small Intestine Submucosa Powder Impregnated

- Poly(L-lactide) scaffolds: The Application for Tissue Engineered Bone and Cartilage,” *Macromolecular Research* 10(3), 158-167 (2002).
38. A.J. Salgado, O.P. Coutinho, R.L. Reis, “Bone Tissue Engineering: State of the Art and Future Trends,” *Macromolecular Bioscience* 4(8), 743-765 (2004).
 39. M Isobe, Y. Yamazaki, S. Oida, K. Ishihara, N. Nakabayashi, T. Amagasa, “Bone morphogenic protein encapsulated with a biodegradable and biocompatible polymer,” *Journal of Biomedical Materials Research* 32(3), 433-438 (1996).
 40. H. Liu, T.J. Webster, “Ceramic/polymer nanocomposites with tunable drug delivery capability at specific disease sites,” *Journal of Biomedical Materials Research Part A* 93A(3), 1180-1192 (2009).
 41. G. Khang, J.M. Rhee, J.K. Jeong, J.S. Lee, M.S. Kim, S.H. Cho, H. B. Lee, “Local Drug Delivery System Using Biodegradable Polymers,” *Macromolecular Research* 11(9), 207-223 (2003).
 42. M. Kato, H. Toyoda, T. Namikawa, M. Hoshino, H. Terai, S. Miyamoto, K. Takaoka, “Optimized use of a biodegradable polymer as a carrier material for the local delivery of recombinant human bone morphogenetic protein-2 (rhBMP-2),” *Biomaterials* 27(9), 2035-2041 (2006).
 43. Froschle, L. J. Mahlitz, H.U. Langendorff, e. Achilles, J. Pollock, K.H. Jungbluth, “Release of daunorubicin from polymethylmethacrylate for the improvement of the local growth control of bone metastasis animal experiments,” *Anticancer Research* 17(2A), 995-1002 (1997).
 44. D.L. Bartel, V.L. Bicknell, T.M. Wright, “The effect of conformity , thickness, and material on stresses in ultra-high molecular weight components for total joint replacement,” *The Journal of Bone and Joint Surgery* 68(7), 1041-1051 (1986).
 45. A. Balko, G.J. Piasecki, D.M. Shah, W.I. Carney, R.W. Hopkins, B.T. Jackson, “Transfemoral placement of intraluminal polyurethane prosthesis for abdominal aortic aneurysm,” *Journal of Surgical Research* 40(4), 305-309 (1986).
 46. J.M. Bello, L.A. Contreras, G. Pascual, J. Buja, “Evaluation of the acute scarring response to the implant of different types of biomaterial in the abdominal wall,” *Journal of Materials Science: Materials in Medicine* 11(1), 25-29 (2000).
 47. S.H. Teoh, “Fatigue of biomaterials: a review,” *International Journal of Fatigue* 22(10), 825-837 (2000).
 48. S.B. Kim, Y.J. Kim, T.L. Yoon, S.A. Park, I.H. Cho, E.J. Kim, I.A. Kim, J.-W. Shin, “The characteristics of a hydroxyapatite-chitosan-PMMA bone cement,” *Biomaterials* 25(26), 5715-5723 (2004).

49. S. Shinzato, M. Kobayashi, W.F. Mousa, M. Kamimura, M. Neo, Y. Kitamura, T. Kokubo, T. Nakamura, "Bioactive polymethyl methacrylate-based bone cement: Comparison of glass beads, apatite- and wollastonite-containing glass-ceramic, and hydroxyapatite fillers on mechanical and biological properties," *Journal of Biomedical Materials Research* 51(2), 258-272 (2000).
50. P. Bracco, V. Brunella, L. Trossarelli, A. Coda, F. Botto-Micca, "Comparison of polypropylene and polyethylene terephthalate (Dacron) meshes for abdominal wall hernia repair: A chemical and morphological study," *Hernia* 9(1), 51-55 (2005).
51. K. Fujihara, Z.-M. Huang, S. Ramakrishna, K. Satknanantham, H. Hamada, "Performance study of braided carbon/PEEK composite compression bone plates," *Biomaterials* 24(15), 2661-2667 (2003).
52. S.M. Kurtz, J.N. Devine, "PEEK biomaterials in trauma, orthopedic, and spinal implants," *Biomaterial* 28(32), 4845-4869 (2007).
53. L. Claes, W. Huttner, R. Weiss, "Mechanical properties of carbon fibre reinforced polysulfone plates for internal fracture fixation," *Biological and Biomechanical Performance of Biomaterials, Proceedings of the Fifth European Conference on Biomaterials; Paris, France* 81-86 (1986).
54. K.P. Andriano, Y. Tabata, Y. Ikada, J. Heller, "In vitro and in vivo comparison of bulk and surface hydrolysis in absorbable polymer scaffolds for tissue engineering," *Journal of Biomedical Materials Research* 48(5), 602-612 (1999).
55. J.M. Karp, M.S. Shoichet, J.E. Davies, "Bone formation on two-dimensional poly(DL-lactide-co-glycolide) (PLGA) films and three-dimensional PLGA tissue engineering scaffolds in vitro," *Journal of Biomedical Materials Research* 64A(2), 388-396 (2003).
56. T. Ren, J. Ren, X. Jia, K. Pan, "The bone formation in vitro and mandibular defect repair using PLGA porous scaffolds," *Journal of Biomedical Materials Research* 74A(4), 562-569 (2005).
57. J.P. Fisher, J.W.M. Vehof, D. Dean, J.P.C.M. van der Waerden, T.A. Holland, A.G. Mikos, J.A. Jansen, "Soft and hard tissue response to photocrosslinked poly(propylene fumarate) scaffolds in a rabbit model," *Journal of Biomedical Materials Research* 59(3), 547-556 (2002).
- 58.
59. E.T. Middleton, C.J. Rajaraman, D.P. O'Brien, S.M. Doherty, A.D. Taylor, "The safety and efficacy of vertebroplasty using Cortoss cement in a newly established vertebroplasty service," *British Journal of Neurosurgery* 22(2), 252-256 (2008).

60. D.H. Kohn, M. Sarmadi, J.I. Helman, P.H. Krebsbach, "Effects of pH on human bone marrow stromal cells *in vitro*: Implications for tissue engineering of bone," *Journal of Biomedical Materials Research* 60(2), 292-299 (2002).
61. J.E. Eastoe, B. Eastoe, "The organic constituents of mammalian compact bone," *Biochemical Journal* 57(3), 453-459 (1954).
62. H.A. Lowenstam, S. Weiner, *On Biomineralization*, pp. 144-67, New York: Oxford University Press (1989).
63. S. Weiner, P.A. Price, "Disaggregation of bone into crystals," *Calcified Tissue International* 39(6), 365-375 (1986).
64. J.-Y. Rho, L. Kuhn-Spearing, P. Zioupos, "Mechanical properties and the hierarchical structure of bone," *Medical Engineering & Physics* 20(2), 92-102 (1998).
65. S. Weiner, H.D. Wagner, "The material bone: Structure-mechanical function relations," *Annual Review of Materials Science* 28, 271-298 (1998).
66. S. Saber-Samandari, K A. Gross, "Micromechanical properties of single crystal hydroxyapatite by nanoindentation," *Acta Biomaterialia* 5(6), 2206-2212 (2009).
67. K.A. Piez, "Cross-linking of collagen and elastin," *Annual Review of Biochemistry* 37, 547-570 (1968).
68. A. Miller, S.B. Parker, "Collagen: The organic matrix of bone [and discussion]," *Philosophical Transactions of the Royal Society B* 304, 455-477 (1984).
69. A.J. Hodge, J.A. Petruska, in *Aspects of Protein Structure* (ed. Ramachandran, G. N.) 289-300 (Academic, New York, 1963)
70. J. S. Nyman, A. Roy, X. Shen, R.L. Acuna, J.H. Tyler, X. Wang, "The influence of water removal on the strength and toughness of cortical bone," *Journal of Biomechanics* 39(5), 931-938 (2006).
71. E.P. Katz, S.T. Li, "The intermolecular space of reconstituted collagen fibrils," *Journal of Molecular Biology* 73(3), 351-369 (1973).
72. R.J. Kelm, N.A. Swords, T. Orfeo, K.G. Mann, "Osteonectin in matrix remodeling. A plasminogen-osteonectin-collagen complex." *The Journal of Biological Chemistry* 269(48), 30147-30153 (1994).
73. T. Reichert, S. Storkel, K. Becker, L.W. Fisher, "The role of osteonectin in human tooth development – An immunohistological study," *Calcified Tissue International* 50(5), 468-472 (1992).

74. J.P. Gorski, "Biom mineralization of bone: A fresh view of the roles of non-collagenous proteins," *Frontiers in Bioscience* 16,259802621 (2011).
75. V. Ziv, H.D. Wagner, S. Weiner, "Microstructure-microhardness relations in parallel-fibred and lamellar bone," *Bone* 18(5), 417-428 (1996).
76. X. Su, K. Sun, F.Z. Cui, W.J. Landis, "Organization of apatite crystals in human woven bone," *Bone* 32, 150-162 (2003).
77. S. Weiner, T. Arad, I. Sabanay, B. Geiger, "Rotated plywood structure of primary lamellar bone in the rat: Orientations of the collagen fibril arrays," *Bone*, 20(6), 509-514 (1997).
78. R.A. Wang, S. Weiner, "Human root dentin: Structural anisotropy and Vickers microhardness isotropy," *Connective Tissue Research* 39(4), 269-279 (1998).
79. K.M. Hannah, C.D.L. Thomas, J.G. Clement, F. De Carlo, A.G. Peele, "Bimodal distribution of osteocyte lacunar size in the human femoral cortex as revealed by micro-CT," *Bone* 47(5), 866-871 (2010).
80. J.Y. Rho, P. Zioupos, J.D. Currey, G.M. Pharr, "Variations in the individual thick lamellar properties within osteons by nanoindentation", *Bone* 25(3), 295-300 (1999).
81. R.D. Crofts, T.M. Boyce, R.D. Bloebaum, "Aging changes in osteon mineralization in the human femoral neck," *Bone* 15(2), 147-152 (1994).
82. P.-Y. Chen, J. McKittrick, "Compressive mechanical properties of demineralized and deproteinized cancellous bone," *Journal of the Mechanical Behavior of Biomedical Materials* 4(7), 961-973 (2011).
83. E. Novitskaya, P.-Y. Chen, S. Lee, A. Castro-Ceseña, G. Hirata, V. Lubarda, J. McKittrick, "Anisotropy in the compressive mechanical properties of bovine cortical bone and the mineral and protein constituents," *Acta Biomaterialia* 7(8), 3170-3177 (2011).
84. E.F. Morgan, H.H. Bayraktar, T.M. Keaveny, "Trabecular bone modulus-density relationships depend on anatomic site," *Journal of Biomechanics* 36(7), 897-904 (2003).
85. L.J. Gibson "The mechanical behavior of cancellous bone," *Journal of Biomechanics* 18(5), 317-328 (1985).
86. T.M. Keaveny, E.F. Morgan, G.L. Niebur, O.C. Yeh, "Biomechanics of trabecular bone," *Annual Review of Biomedical Engineering* 3(1), 307-333 (2001).
87. J.M. Wozney, "The bone morphogenetic protein family and osteogenesis," *Molecular Reproduction and Development* 32(2), 160-167 (1992).

88. Y. Kuboki, H. Takita, D. Kobayashi, E. Tsuruga, M. Inoue, M. Murata, N. Nagai, Y. Dohi, H. Ohgushi, "BMP-induced osteogenesis on the surface of hydroxyapatite with geometrically feasible and nonfeasible structures: topology of osteogenesis," *Journal of Biomedical Materials Research* 39(2), 190-199 (1998).
89. Y.S. Chang, H.O. Gu, M. Kobayashi, M. Oka, "Influence of various structure treatments on histological fixation of titanium implants," *Journal of Arthroplasty* 13(7), 816-825 (1998).
90. J.X. Lu, F.K. Anselme, P. Hardouin, A. Gallur, M. Descamps, B. Thierry, "Role of interconnections in porous bioceramics on bone recolonization in vitro and in vivo," *Journal of Materials Science* 10(2), 111-120 (1999).
91. S.F. Hulbert, F.A. Young, R.S. Mathews, J.J. Klawitter, C.D. Talbert, F.H. Stelling, "Potential of ceramic materials as permanently implantable skeletal prostheses," *Journal of Biomedical Materials Research* 4(3), 433-456 (1970).
92. B.S. Chang, C.K. Lee, K.S. Hong, H.J. Youn, H.S. Ryu, S.S. Chung, K.W. Park, "Osteoconduction at porous hydroxyapatite with various pore configuration," *Biomaterials* 21(12), 1291-1298 (2000).
93. R.M. Pillar, H.U. Cameron, A.G. Binnington, J. Szivek, I. Macnab, "Bone ingrowth and stress shielding with a porous surface coated fracture fixation plate," *Journal of Biomedical Materials Research* 13(5), 799-810 (1979).
94. C.A. Engh, J.D. Bobyn, A.H. Glassman, "Porous-coated hip-replacement – The factors governing bone ingrowth, stress shielding, and clinical results," *Journal of bone and Joint Surgery – British Volume* 69(1), 45-55 (1987).
95. V.K. Goel, T.H. Lim, J. Gwon, J.Y. Chen, J.M. Winterbottom, J.B. Park, J.N. Weinstein, J.Y. Ahn, "Effects of rigidity of an internal fixation device – A comprehensive biomechanical investigation," *Spine* 16(3), S155-S161 (1991).
96. R. Huiskes, H. Weinans, B. Vanrietbergen, "The relationship between stress shielding and bone resorption around total hip stems and the effects of flexible materials," *clinical Orthopaedics and Related Research* (274), 124-134 (1992).
97. B. Vanrietbergen, R. Huiskes, H. Weinans, D.R. Sumner, T.M. Turner, J.O. Galante, "The mechanism of bone remodeling and resorption around press-fitted THA stems," *Journal of Biomechanics* 26(4-5), 369-382 (1993).
98. CA Engh, JP Jr Hooten, KF Zettl-Schaffer, M Ghaffarpour, TF McGovern, GE Macalino, BA Zicat, "Porous-coated hip replacement," *The Journal of Bone and Joint Surgery* 69(1), 45-55 (1987).
99. M. Azami, F. Moztarzadeh, M. Tahriri, "Preparation, characterization and mechanical properties of controlled porous gelatin/hydroxyapatite nanocomposite through layer

- solvent casting combined with freeze-drying and lamination techniques,” *Journal of Porous Materials* 17(3), 313-320 (2010).
100. S. Blindow, M. Pulkin, D. Koch, “Hydroxyapatite/SiO₂ Composites via Freeze Casting for Bone Tissue Engineering,” *Advanced Engineering Materials* 11(11), 875-884 (2009).
 101. S. Deville, E. Saiz, A.P. Tomsia, “Freeze casting of hydroxyapatite scaffolds for bone tissue engineering,” *Biomaterials* 27(32), 5480-5489 (2006).
 102. Q. Fu, M.N. Mohamed, F. Dogan, B.S. Bal, “Freeze-cast hydroxyapatite scaffolds for bone tissue engineering applications,” *Biomedical Materials* 3(2), (2008).
 103. Q. Fu, M.N. Rahaman, B.S. Bal, R.F. Brown, “Proliferation and Function of MC3T3-E1 cells on Freeze-Cast Hydroxyapatite Scaffolds with Oriented Pore Architectures,” *Journal of Materials Science – Materials in Medicine* 32(2), 86-95 (2009).
 104. E.J. Lee, Y.H. Koh, B.H. Yoon, H.E. Kim, H.W. Kim, “Highly porous hydroxyapatite bioceramics with interconnected pore channels using camphene-based freeze casting,” *Materials Letters* 61(11-12), 2270-2273 (2007).
 105. T. Moritz, H.-J. Richter, “Ceramic Bodies with Complex Geometries and Ceramic Shells by Freeze Casting Using Ice as Mold Material,” *Journal of the American Ceramic Society*, 89(8), 2394-2398 (2006).
 106. Y. Suetsugu, Y. Hotta, M. Iwasashi, M. Sakane, M. Kikuchi, T. Ikoma, T. Higaki, N. Ochiai, J. Tanaka, “Structural and Tissue Reaction Properties of Novel Hydroxyapatite Ceramics with Unidirectional Pores,” *Key Engineering Materials* 330-332, 1003-1006 (2007).
 107. T.Y. Yang, J.M. Lee, S.Y. Yoon, H.C. Park, “Hydroxyapatite scaffolds processed using a TBA-based freeze-gel casting/polymer sponge technique,” *Journal of Materials Science-Materials in Medicine* 21(5), 1495-1502 (2010).
 108. B.H. Yoon, C.S. Park, H.E. Kim, Y.H. Koh, “In-situ fabrication of porous hydroxyapatite (HA) scaffolds with dense shells by freezing HA/camphene slurry,” *Materials Letters* 62(10-11), 1700-1703 (2008).
 109. Y. Zhang, K. Zuo, Y.-P. Zeng, “Effects of gelatin addition on the microstructure of freeze-cast porous hydroxyapatite ceramics,” *Ceramics International* 35, 2151-2154 (2009).
 110. K.H. Zuo, Y.P. Zeng, D.L. Jiang, “Effect of polyvinyl alcohol additive on the pore structure and morphology of the freeze-cast hydroxyapatite ceramics,” *Materials Science and Engineering: C* 30(2), 283-287 (2010).

111. K.H. Zuo, Y.A. Zhang, Y.P. Zeng, D.L. Jiang, "Pore-forming agent induced microstructure evolution of freeze casted hydroxyapatite," *Ceramics International* 37(1), 407-410 (2011).
112. S. Deville, "Freeze-Casting of Porous Ceramics: A Review of Current Achievements and Issues," *Advanced Engineering Materials* 10(3), 155-169 (2008).
113. Wegst, U.G.K., Schecter, M., Donius, A.E., and P.M. Hunger, "Biomaterials by freeze casting," *Philosophical Transactions of the Royal Society A* 368, 2099-2121 (2010).
114. M.C. Flemings, *Solidification Processing*, 1st ed. (McGraw-Hill, New York, 1974) p. 100.
115. S. Deville, E. Saiz, A.P. Tomsia, "Ice-templated porous alumina structures," *Acta Materialia* 55(6), 1965-1974 (2007).
116. W.L. Li, J.Y. Walz, "Freeze casting of porous materials: review of critical factors in microstructure evolution," *International Materials Reviews* 57(1), 37-60 (2012).
117. Y. Zhang, K. Zuo, Y.-P. Zeng, "Effects of gelatin addition on the microstructure of freeze-cast porous hydroxyapatite ceramics," *Ceramics International* 35(6), 2151-2154 (2009).
118. Q. Fu, M.N. Rahaman, R. Dogan, B.S. Bal, "Freeze casting of porous hydroxyapatite scaffolds. I. processing and general microstructure," *Journal of Biomedical Materials Research Part B: Applied Biomaterials* 86B(1), 125-135 (2008).
119. K. Araki, J.W. Halloran, "Porous ceramic bodies with interconnected pore channels by a novel freeze casting technique," *Journal of the American Ceramic Society* 88(5), 1108-1114 (2005).
120. Y.M. Soon, K.H. Shin, Y.H. Koh, J.H. Lee, H.E. Kim, "Compressive strength and processing of camphene-based freeze cast calcium phosphate scaffolds with aligned pore," *Materials Letters* 63(17), 1548-1550 (2009).
121. Y. Taniguchi, T. Tamaki, H. Oura, H. Hashizume, A. Minamide "Sintered bone implantation for the treatment of benign bone tumours in the hand," *Journal of Hand Surgery* 24B(1), 109-112 (1999).
122. J. Li, Z. Lin, Q. Zheng, X. Guo, S. Lan, S. Liu, S. Yang, "Repair of rabbit radial bone defects using true bone ceramics combined with BMP-2-related peptide and type I collagen," *Materials Science and Engineering: C* 30(8), 1272-1279 (2010).

123. A. Minamide, M. Kawakami, H. Hashizume, R. Sakata, T. Tamaki, "Evaluation of carriers of bone morphogenetic protein for spinal fusion," *Spine* 26(8), 933-939 (2001).
124. A. Minamide, M. Kawakami, H. Hashizume, R. Sakata, M. Yoshida, T. Tamaki, "Experimental study of carriers of bone morphogenetic protein used for spinal fusion," *Journal of Orthopaedic Science* 9(2), 142-151 (2004).
125. S. Deb, M. Wang, E. Tanner, W. Bonfield, "Hydroxyapatite-polyethylene composites: effect of grafting and surface treatment of hydroxyapatite," *Journal of Materials Science: Materials in Medicine* 7(4), 191-193 (1996).